Journal of Asian Earth Sciences 259 (2024) 105910

Contents lists available at ScienceDirect

Journal of Asian Earth Sciences

journal homepage: www.elsevier.com/locate/jseaes

Fe-(oxyhydr)oxide participation in REE enrichment in early Cambrian phosphorites from South China: Evidence from in-situ geochemical analysis

Haiying Yang [a,c,d], Zhifang Zhao [a,c,d,*], Haifeng Fan [b], Min Zeng [a,c,d], Jiafei Xiao [b], Xiqiang Liu [b], Shengwei Wu [b], Jiangqin Chao [a,c,d], Yong Xia [b]

[a] School of Earth Sciences, Yunnan University, Kunming 650500, China
[b] State Key Laboratory of Ore Deposit Geochemistry, Institute of Geochemistry, Chinese Academy of Sciences, Guiyang 550081, China
[c] Yunnan International Joint Laboratory of China-Laos-Bangladesh-Myanmar Natural Resources Remote Sensing Monitoring, Kunming 650500, China
[d] MNR Key Laboratory of Sanjiang Metallogeny and Resources Exploration & Utilization, Kunming 650051, China

ARTICLE INFO

Keywords:
REE-rich phosphorite
Early Cambrian
In-situ analysis
Fe/Mn (oxyhydr)oxides
South China

ABSTRACT

Marine phosphorites have shown extraordinary REE potential. Enrichment mechanisms have been investigated as yet, however, the roles of Fe/Mn (oxyhydr)oxides in REE enrichment were poorly known. In this paper, we report new data for early Cambrian phosphorites in South China with a particular focus on REE enrichment and Fe-redox cycling. Phosphorites from the Cambrian Gezhongwu occur in the upper and lower units. The phosphorites contain a large number of of Fe (oxyhydr)oxides, especially those in the upper unit. SEM and laser Raman show that Fe (oxyhydr)oxides have a gray rim and a bright core, attributed to transformation from hematite to goethite during the weathering. In-situ elemental analyses show Fe (oxyhydr)oxides have PAAS-normalized REE patterns depleted in LREE and enriched in HREE with negative to positive Eu anomalies and positive Y anomalies. However, two patterns are clearly distinguished according to Ce anomalies and these are related to the origins of Fe-(oxyhydr)oxides: hydrothermal Fe (oxyhydr)oxides with negative Ce anomalies and hydrogenic ones with positive Ce anomalies. The role of Fe (oxyhydr)oxides played in REE enrichment was controlled by Fe-redox pumping. In this process, Fe (oxyhydr)oxides adsorbed REEs in oxic water columns; after precipitating to suboxic/anoxic conditions, the absorbed REEs were released into porewater. Francolites subsequently formed and captured REEs during early diagenesis. Even though additional evidence is required, our investigations were significant in conforming the origins of Fe/Mn (oxyhydr)oxides and their role in REE enrichment in marine phosphorites.

1. Introduction

Rare earth elements plus Y (REEs) are widely used in new technology industries, which include national defense, military, aerospace, clean energy, and unique materials (Balaram, 2019). REEs have been listed as key mineral resources in most countries and are of great importance in studying REE mineralization. Typical REE deposits come from carbonatite deposits and alkaline rocks/alkaline granites in areas such as Bayan Obo, Yinachang, and Mianning-Dechang; these deposits provide light REEs (LREEs, La-Nd) (Ye et al., 2013; Li and Zhou, 2015; Fan et al., 2016b; Liu et al., 2019). In addition, supergene weathering type/ion adsorption clay-type (Bao and Zhao, 2008; Li et al., 2017; Wang et al., 2018; Li et al., 2019; Zhou et al., 2020) and placer type (Yuan et al., 2012) REE deposits provide middle (MREEs) and heavy REEs (HREEs). Sedimentary deposits, such as deep-sea muds and phosphorites, have recently been reported as sources of REEs and have unusually enriched amounts of MREEs and HREEs (Kato et al., 2011; Emsbo et al., 2015). Notably, sedimentary phosphorite deposits rich in REEs occur worldwide in areas like Jordan, North America, South China, Australia, and South Africa (Cook, 1992; Pufahl and Hiatt, 2012). Furthermore, REE-enriched phosphorites formed in multiple geological periods, with the Paleozoic Era serving as the most important REE-enriched phosphorite formation stage (Emsbo et al., 2015). For example, the Upper Ordovician phosphorites from Love Hollow, Illinois contained REE concentrations (∑REE) of up to 5400 ppm; the ∑REE of the Upper Devonian phosphorites from Kentucky, New York approached 18000 ppm (Kato et al., 2011; Emsbo et al., 2015). Therefore, phosphorites could serve as a new REE resource and probably meet global REE demands, especially

* Corresponding author.
E-mail addresses: zhaozhifang@ynu.edu.cn, zzf_1002@162.com (Z. Zhao).

https://doi.org/10.1016/j.jseaes.2023.105910
Received 16 February 2023; Received in revised form 28 October 2023; Accepted 31 October 2023
Available online 5 November 2023

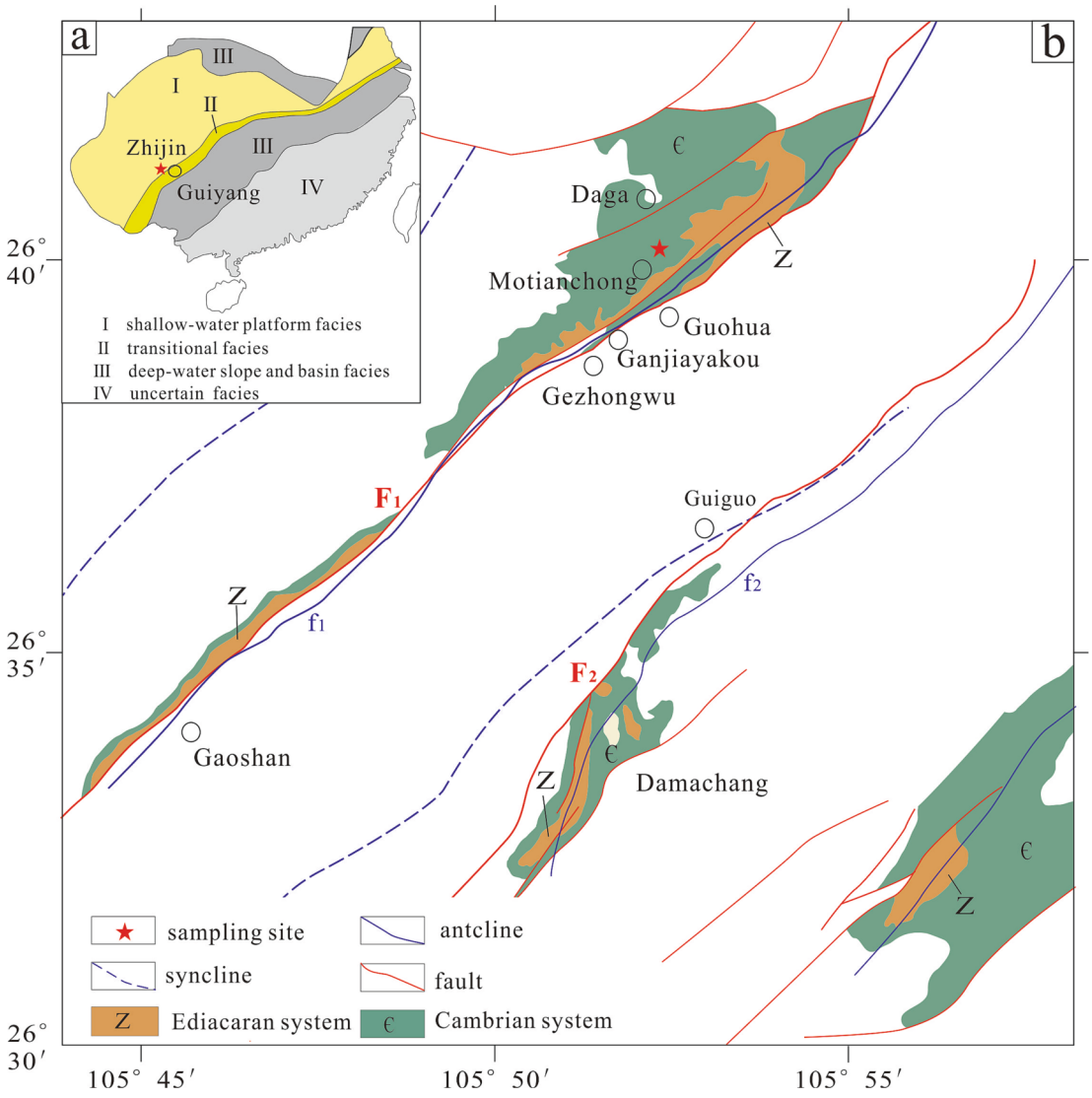

Fig. 1. (a) Simplified paleogeographic map of South China during the early Cambrian, modified after Steiner et al. (2001). (b) Geological map of the Zhijin phosphorite deposit.

for scarce HREEs (Kato et al., 2011; Emsbo et al., 2015).

The mineralization mechanisms of REE-enriched phosphorites have attracted significant research attention recently. Paleogeographic locations, continental REE input, hydrothermal activity, redox conditions, biological activity, and diagenetic process have been proposed as possible controls (Emsbo et al., 2015; Pufahl and Groat, 2017; Francovschi et al., 2020; Frei et al., 2021; Yang et al., 2021a; Yang et al., 2021b; Zhang et al., 2022). However, there is no consensus on the REE enrichment mechanism. For example, diagenetic uptake of REEs into francolites was generally accepted for REE enrichment in phosphorites (Kocsis et al., 2010; Lumiste et al., 2019; Francovschi et al., 2020); however, the homogeneous distribution of REEs in Zhijin collophane and francolites contradicted this (Yang et al., 2021b). Secondly, some researchers suggested that REE biosorption caused MREE enrichment in Zhijin phosphorite (Wright et al., 1987; Zhang et al., 2003; Frei et al., 2021); whereas, Xia'An (early Cambrian) and Weng'An (Sinian) phosphorites with high productivity yielded very low REE concentrations. This indicated that biosorption might not play critical role in REE enrichment (Yang et al., 2021b; Zhang et al., 2022). Additionally, Fe-pumping driven by fluctuating redox conditions in seawater and porewater was proposed to explain extraordinary REE enrichment in phosphorites (Jarvis et al., 1994; She et al., 2013; Zhang et al., 2022). However, Kunyang phosphorites formed under the redox conditions consistent with Zhijin showed low ∑REE (<250 ppm) (Wen et al., 2011; Liu and Zhou, 2017). Therefore, in sedimentary REE-rich phosphorites, the specific process of different controls in REE enrichment remain unclear.

Based on a Fe-pumping mode, Fe/Mn (oxyhydr)oxides were thought to play significant roles in francolite formation and REE enrichment both in deep-sea muds and shallow phosphorite (Takahashi et al., 2015; Kashiwabara et al., 2018; Yang et al., 2022a). Research suggested that hydrothermal Fe/Mn (oxyhydr)oxides contributed as "the initial carriers" due to their high adsorptive abilities (Takahashi et al., 2015; Kashiwabara et al., 2018). In an experimental model, Bau et al. (1996) concluded that MnO_2 preferentially absorbed MREE, as well as FeOOH. In addition, REE absorption experiments showed that REEs scavenged by MnO_2 and Fe oxyhydroxide increased with solution pH (Ohta and Kawabe, 2001). In natural sedimentary conditions, REEs absorbed by Fe/Mn (oxyhydr)oxides eventually affixed to francolites via an adsorption–desorption equilibrium by oxidation transformation during early diagenesis (Poulton and Canfield, 2006; Zhang et al., 2022). These research efforts indicated that Fe/Mn (oxyhydr)oxides played an important role in REE adsorption not only in experiments but also in natural sediments. Nevertheless, several questions remained, such as the

Table 1
Major elemental compositions of early Cambrian phosphorite from the Zhijin deposit, Central Guizhou, South China (wt.%).

Samples	lithology	Al_2O_3	CaO	F	TFe_2O_3	K_2O	MgO	MnO_2	P_2O_5	SiO_2	SO_3	LOI
ZK-130	quartz siltstone	8.41	2.56	–	2.34	2.12	2.17	0.04	0.20	75.42	0.06	5.89
ZK-142.8	siliceous dolomitic phosphorite	1.64	34.00	1.40	1.59	0.52	13.10	0.14	11.55	7.34	0.82	28.63
ZK-146.8	siliceous phosphatic dolomite	0.45	29.20	0.40	1.02	0.14	17.85	0.26	2.78	9.64	0.14	39.07
ZK-147.4	siliceous phosphatic dolomite	1.71	32.10	1.00	1.44	0.56	14.35	0.23	8.16	7.69	0.75	32.58
ZK-149.2	siliceous dolomitic phosphorite	1.08	33.40	1.30	3.06	0.35	11.40	0.22	12.65	10.05	1.58	24.56
ZK-150.1	siliceous phosphatic dolomite	0.50	29.30	0.60	2.64	0.16	15.70	0.46	4.58	11.10	1.26	34.88
ZK-151.9	siliceous phosphatic dolomite	1.42	29.40	0.80	2.95	0.46	13.50	0.52	6.41	11.50	0.89	31.94
ZK-152.5	siliceous phosphatic dolomite	0.88	28.00	0.60	3.26	0.29	14.60	0.57	4.12	13.96	1.02	33.86
ZK-153.8	siliceous phosphatic dolomite	0.33	29.20	0.80	2.68	0.12	12.80	0.39	6.78	15.65	1.10	30.18
ZK-154.6	siliceous dolomitic phosphorite	1.30	29.00	1.00	2.39	0.41	11.35	0.29	9.02	15.80	0.77	28.03
ZK-155.8	siliceous phosphatic dolomite	0.96	28.40	0.60	2.17	0.31	15.50	0.30	4.00	12.90	0.51	35.11
ZK-156.5	siliceous dolomitic phosphorite	0.30	31.00	0.90	1.88	0.10	14.10	0.20	8.18	11.85	0.05	31.73
ZK-159.5	phosphorite	0.27	39.10	1.80	1.25	0.08	9.87	0.23	17.35	6.42	0.07	23.93
ZK-160.7	dolomitic phosphorite	0.45	39.60	1.70	0.98	0.15	12.25	0.13	15.35	2.32	0.26	28.24
ZK-161.5	phosphatic dolomite	0.21	33.70	0.80	0.77	0.07	16.00	0.13	7.09	3.58	0.08	37.29
ZK-163.1	dolomitic phosphorite	0.69	35.90	1.20	0.67	0.22	13.90	0.09	11.40	4.46	0.19	31.77
ZK-163.9	dolomitic phosphorite	0.33	35.30	1.10	0.55	0.11	15.05	0.10	9.79	4.39	0.05	34.05
ZK-164.5	dolomitic phosphorite	0.36	34.20	1.10	0.51	0.11	15.20	0.10	9.30	6.55	0.05	33.73
ZK-165.2	phosphorite	0.38	45.60	2.80	0.60	0.13	5.33	0.04	27.40	5.52	0.57	13.15
ZK-166.8	phosphorite	0.78	43.50	2.70	0.88	0.26	5.53	0.05	26.00	5.80	0.59	14.22
ZK-168.5	phosphorite	0.95	34.50	1.50	0.87	0.38	10.00	0.05	14.70	13.85	1.00	22.50
ZK-168.9	dolomite	0.39	29.00	0.20	0.74	0.12	20.40	0.18	0.16	4.86	0.37	44.54
ZK-170	dolomite	0.52	29.60	–	0.35	0.19	20.20	0.08	0.71	4.15	0.39	43.81

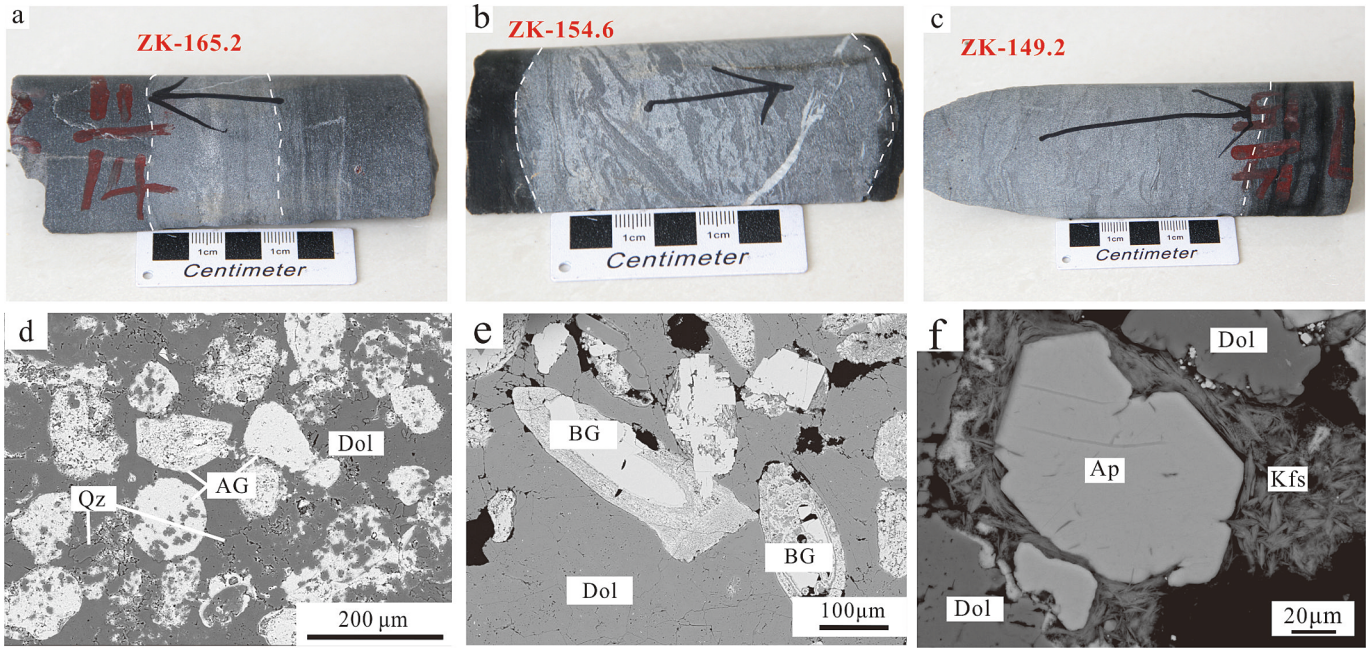

Fig. 2. Characteristics of phosphorite hand specimens (a)-(c) and francolites (d)-(f) from the Gezhongwu Formation, early Cambrian in Zhijin phosphorite, South China. (a) massive phosphorite; (b), (c) banded phosphorite; (d) biodetritus;(e) abiogenic grains; and (f) francolite individuals. Abbreviation: AG: abiogenic grain; BG: biogenic grain; Qz: quartz; Kfs: K-feldspar; Dol: dolomite; Ap: apatite.

involvement of Fe/Mn (oxyhydr)oxides in phosphorite formation and the REE fractionation between Fe/Mn (oxyhydr)oxides and francolites. These questions limited further understanding of REE transformations and enrichments in marine phosphorite.

One of the earliest worldwide phosphogenesis occurred during the early Cambrian (~541–529), Paleozoic Era (Cook and Shergold, 1984). During this time, South China developed phosphorites at the shallow carbonate platform, including large-scale phosphorite (such as Zhijin and Kunyang) at the shelf and small-scale phosphate concretions at the near-slope (Steiner et al., 2007; Zhu et al., 2007). Among them, the Zhijin phosphorites contained higher ∑REE (>1000 ppm), attracting abundant research interest focused on REE enrichment mechanisms. Three kinds of phosphate minerals (authigenic, biogenetic, and amorphous) were found in our previous research (Yang et al., 2021a; Yang et al., 2021b). Correspondingly, Fe/Mn (oxyhydr)oxides, organisms/organic matters, and diagenesis played important roles, particularly in P and REE carriers. As for organisms/organic matter, Wu et al., (2022b) concluded their effects on REE enrichment according to heavier $\delta^{13}C_{carb}$, lighter $\delta^{13}C_{org}$, and higher TOC in Zhijin phosphorites as compared to Kunyang phosphorites. REEs were released into the pore-water due to anaerobic oxidation of organic matter at the seawater-sediment interface, which finally resulted in REE enrichment of Zhijin phosphorites (Wu et al., 2022b). Regarding Fe/Mn (oxyhydr)oxides, Zhang et al. (2022) conducted an isotopic study of Zn and Fe in Zhijin, Kunyang, and Xia'an phosphorites and suggested that frequent Fe redox cycling as crucial factor for REE transportation, release, and

Table 2
Trace elemental compositions of early Cambrian phosphorite from the Zhijin deposit, Central Guizhou, South China (ppm).

Samples	Li	Be	Sc	V	Cr	Ni	Cu	Zn	Ga	Ge	As	Rb	Sr	Zr	Sb	Ba	Pb	Th	U
ZK-91	36.50	3.86	16.00	198.00	114.00	62.80	48.50	111.00	24.60	1.96	4.49	132.00	170.00	179.00	1.58	730.00	37.20	13.30	5.84
ZK-108	30.70	2.76	12.40	140.00	80.20	50.20	45.50	96.60	18.80	1.75	2.09	106.00	176.00	141.00	0.83	666.00	23.20	11.30	3.63
ZK-118	32.30	3.64	15.30	221.00	94.50	76.50	51.50	106.00	23.00	1.99	3.92	127.00	115.00	153.00	1.40	689.00	38.40	13.00	7.04
ZK-130	27.90	3.39	15.60	181.00	96.60	56.70	61.00	100.00	23.20	1.98	3.88	129.00	112.00	158.00	1.19	734.00	46.00	12.70	6.11
ZK-142.8	16.00	1.69	3.28	70.00	34.00	483.00	14.70	500.00	10.60	1.13	31.77	52.10	44.50	238.00	11.30	235.00	18.80	7.85	6.69
ZK-146.3	19.00	2.82	0.76	16.90	19.10	19.10	8.16	36.40	5.32	0.68	10.25	11.80	469.00	52.50	18.80	253.00	76.40	5.78	4.72
ZK-146.8	4.56	0.60	–	2.87	2.32	15.20	1.93	127.00	1.34	0.25	3.88	3.26	180.00	6.53	2.50	75.90	496.00	0.85	1.09
ZK-147.4	13.20	1.55	2.12	12.60	8.49	16.90	4.05	16.30	3.83	0.46	3.88	12.50	381.00	25.60	4.97	214.00	36.10	2.30	2.72
ZK-148.3	8.54	0.32	0.93	5.73	4.90	15.80	3.37	10.10	1.98	0.25	4.03	7.01	229.00	11.60	6.14	370.00	330.00	1.11	1.55
ZK-149.2	24.60	2.10	0.78	8.45	9.74	19.50	9.02	215.00	4.11	0.53	10.12	9.00	558.00	21.30	12.10	263.00	244.00	2.34	3.94
ZK-150.1	7.47	1.03	–	2.91	3.79	13.80	4.37	11.90	1.76	0.29	7.26	3.58	232.00	6.39	6.92	105.00	61.50	0.81	1.49
ZK-150.7	12.60	1.35	–	4.17	3.11	15.90	5.72	4.34	2.21	0.31	3.94	5.84	248.00	9.13	4.81	121.00	30.20	1.00	1.48
ZK-151.2	5.51	0.33	–	3.32	4.90	13.40	3.90	5.70	1.64	0.39	1.76	3.46	210.00	6.34	1.67	91.10	12.70	0.87	1.35
ZK-151.9	19.90	2.27	0.91	12.10	13.00	13.50	8.70	6.28	3.31	0.43	6.03	11.10	275.00	21.10	7.55	199.00	15.30	2.24	3.12
ZK-152.5	14.90	1.16	–	6.06	3.52	112.00	7.89	3.90	1.88	0.32	3.46	6.24	187.00	11.20	4.29	88.20	10.20	1.03	1.58
ZK-153	35.70	2.10	0.39	9.99	10.40	24.50	13.60	5.32	3.76	0.52	6.56	10.20	407.00	19.30	8.21	227.00	25.30	2.48	4.07
ZK-153.8	18.30	2.15	–	2.32	3.75	80.40	6.79	1.45	1.96	0.35	6.25	2.72	327.00	6.35	9.76	153.00	13.60	1.08	2.21
ZK-154.1	4.44	0.74	–	10.10	5.94	22.50	5.53	5.94	1.09	0.35	3.09	5.37	82.80	14.70	5.05	98.70	8.89	1.14	0.94
ZK-154.6	12.80	1.80	1.82	13.80	5.55	32.70	16.90	7.04	3.70	0.51	5.81	8.94	444.00	36.10	12.00	189.00	25.20	3.67	4.28
ZK-155.3	5.85	0.97	0.73	12.30	2.92	30.90	14.60	7.79	2.73	0.32	7.74	6.27	374.00	13.50	17.80	139.00	23.50	2.05	2.66
ZK-155.8	6.53	0.59	0.29	7.35	2.41	21.40	21.80	3.96	1.82	0.37	10.38	6.56	223.00	8.35	13.10	161.00	28.70	1.23	1.59
Mean	**17.01**	**1.77**	**5.09**	**44.81**	**24.91**	**56.99**	**17.03**	**65.81**	**6.79**	**0.72**	**6.69**	**31.43**	**259.25**	**54.24**	**7.24**	**276.28**	**76.25**	**4.20**	**3.24**
δ	**8.34**	**0.75**	**0.93**	**15.62**	**8.03**	**113.21**	**5.56**	**127.31**	**2.25**	**0.21**	**6.79**	**11.33**	**137.76**	**55.01**	**4.97**	**79.24**	**138.13**	**1.93**	**1.59**
Samples	Li	Be	Sc	V	Cr	Ni	Cu	Zn	Ga	Ge	As	Rb	Sr	Zr	Sb	Ba	Pb	Th	U
ZK-156.5	3.84	0.55	0.26	11.80	2.52	24.90	129.00	30.90	1.98	0.49	12.14	2.34	409.00	6.37	21.90	260.00	22.90	2.17	2.72
ZK-157.9	5.29	2.32	0.48	9.86	6.02	30.20	82.40	21.00	2.85	0.46	6.91	2.25	569.00	9.89	40.70	374.00	16.30	2.45	3.52
ZK-158.7	7.71	1.94	1.48	8.25	3.16	26.20	121.00	17.00	3.56	0.67	7.17	2.76	764.00	11.30	15.30	578.00	22.30	3.01	4.45
ZK-159.5	6.85	0.75	0.77	11.30	1.94	16.80	11.50	4.31	3.52	0.54	6.20	1.92	742.00	11.90	17.10	776.00	17.50	2.44	4.42
ZK-160	4.50	1.49	0.88	12.50	4.30	29.00	9.61	3.98	2.28	0.36	6.12	2.46	478.00	10.30	10.20	297.00	15.90	1.87	3.02
ZK-160.7	6.21	1.91	0.57	11.20	2.90	15.80	7.57	3.58	3.19	0.38	4.03	3.00	648.00	18.80	7.80	466.00	15.60	2.42	4.30
ZK-161.5	3.65	1.96	0.43	12.40	7.33	16.40	7.65	7.62	1.60	0.29	3.46	1.57	343.00	7.39	5.71	172.00	9.08	1.42	2.10
ZK-161.9	3.30	1.22	2.63	11.20	3.83	14.50	8.30	8.13	2.06	0.38	3.13	1.45	445.00	7.09	3.14	200.00	7.98	1.59	2.17
ZK-163.1	5.54	2.12	2.10	15.40	3.81	14.50	7.63	4.36	3.04	0.41	3.68	4.98	523.00	18.00	5.14	256.00	11.40	2.85	3.04
ZK-163.9	4.75	1.83	2.48	13.40	4.90	13.50	8.35	6.88	2.32	0.37	3.53	2.36	459.00	8.85	19.20	217.00	9.91	2.01	2.40
ZK-164.5	3.56	1.94	1.94	13.60	3.85	12.10	11.80	8.14	1.99	0.34	3.60	2.47	423.00	8.08	12.90	214.00	8.52	1.75	1.87
ZK-165.2	9.53	3.27	3.26	12.30	5.23	15.90	11.20	1.76	4.94	0.77	4.58	3.06	950.00	22.50	8.41	582.00	17.20	3.80	5.29
ZK-166.2	4.71	1.38	2.62	13.80	4.59	11.90	12.80	4.97	2.25	0.30	2.85	2.75	431.00	12.00	6.79	285.00	11.50	1.80	2.00
ZK-166.8	11.50	2.21	3.87	26.20	9.53	18.30	22.30	8.20	5.37	0.74	6.69	5.91	882.00	38.40	17.20	629.00	68.20	4.65	5.32
ZK-168.5	8.25	1.17	2.94	10.10	8.32	14.10	15.70	5.10	3.72	0.58	6.64	6.40	569.00	27.10	9.47	287.00	22.30	2.91	2.91
Mean	**5.95**	**1.74**	**1.78**	**12.89**	**4.82**	**18.27**	**31.12**	**9.06**	**2.98**	**0.47**	**5.38**	**3.05**	**575.67**	**14.53**	**13.40**	**372.87**	**18.44**	**2.48**	**3.30**
δ	**2.41**	**0.68**	**1.17**	**4.09**	**2.17**	**6.15**	**42.47**	**7.92**	**1.10**	**0.16**	**2.43**	**1.50**	**183.53**	**8.99**	**9.42**	**187.01**	**14.67**	**0.87**	**1.18**
ZK-168.9	1.86	0.54	0.46	29.10	6.62	14.00	3.88	7.70	0.73	0.17	4.05	3.66	43.80	5.50	5.45	22.10	6.73	0.39	0.66
ZK-169.1	2.59	0.66	1.07	41.90	6.61	14.60	3.53	5.52	0.96	0.08	2.26	4.71	34.00	7.06	3.17	19.50	11.00	0.61	0.76
ZK-170	3.07	0.35	0.85	49.70	21.30	17.00	14.80	18.60	1.21	0.13	2.96	5.42	42.20	10.50	10.50	30.70	8.32	0.77	2.29

Table 3
Rare earth element compositions of early Cambrian phosphorite from the Zhijin deposit, Central Guizhou, South China (ppm).

Samples	La	Ce	Pr	Nd	Sm	Eu	Gd	Tb	Dy	Ho	Er	Tm	Yb	Lu	Y	∑REE	Y/Ho	Ce/Ce*	Eu/Eu*
ZK-91	42.50	82.00	9.68	34.00	6.00	1.20	4.90	0.82	5.17	1.19	3.27	0.52	3.06	0.57	31.00	194.89	26.05	0.93	1.04
ZK-108	35.20	69.20	8.34	30.10	6.55	1.43	5.00	0.87	4.93	1.11	2.87	0.47	2.74	0.47	29.10	169.29	26.22	0.93	1.17
ZK-118	38.20	72.90	8.71	31.30	5.61	1.26	4.74	0.85	4.52	1.16	2.99	0.48	2.82	0.49	29.50	176.02	25.43	0.92	1.14
ZK-130	39.70	77.30	9.25	32.20	5.79	1.28	4.79	0.78	4.94	1.11	3.18	0.47	2.97	0.49	30.20	184.25	27.21	0.93	1.13
ZK-142.8	26.50	43.90	4.46	15.60	2.87	0.52	2.59	0.43	2.83	0.64	1.92	0.35	2.00	0.38	18.20	104.98	28.57	0.92	0.89
ZK-146.3	136.00	126.00	32.40	138.00	26.40	5.85	28.01	4.34	27.10	6.43	16.10	1.96	8.33	1.28	197.00	558.19	30.64	0.44	1.00
ZK-146.8	39.10	35.00	7.33	30.00	5.46	1.02	5.22	0.91	5.41	1.35	3.47	0.55	2.73	0.41	56.00	137.95	41.48	0.47	0.89
ZK-147.4	91.30	78.50	19.00	75.40	14.40	3.18	15.04	2.47	15.30	3.71	9.21	1.15	5.36	0.73	127.00	334.76	34.23	0.43	1.00
ZK-148.3	48.40	39.40	7.88	33.10	5.61	2.18	5.97	0.99	6.41	1.65	4.53	0.66	3.38	0.55	69.30	160.71	42.00	0.46	1.74
ZK-149.2	124.00	100.00	25.00	98.80	17.50	3.98	19.37	3.15	19.20	4.71	12.00	1.49	6.84	1.03	170.00	437.06	36.09	0.41	1.00
ZK-150.1	57.00	44.10	9.55	37.10	6.41	1.36	7.06	1.10	7.13	1.76	4.67	0.65	2.98	0.46	80.90	181.33	45.97	0.43	0.93
ZK-150.7	61.00	49.20	10.10	41.40	7.04	1.46	7.86	1.25	7.97	2.09	5.17	0.73	3.57	0.52	85.40	199.36	40.86	0.45	0.91
ZK-151.2	51.30	41.70	8.41	33.20	5.66	1.20	6.34	1.07	6.44	1.66	4.17	0.56	2.91	0.42	72.80	165.03	43.86	0.45	0.93
ZK-151.9	81.60	69.60	15.30	65.10	11.20	2.43	12.25	1.95	11.60	3.02	7.30	0.92	4.19	0.60	119.00	287.06	39.40	0.45	0.96
ZK-152.5	48.90	37.70	8.39	33.80	5.84	1.31	6.10	1.00	6.40	1.59	3.99	0.54	2.59	0.39	71.10	158.53	44.72	0.42	1.02
ZK-153	102.00	84.10	20.40	90.10	16.30	3.75	19.19	2.89	18.80	4.53	11.30	1.40	6.82	0.85	133.00	382.42	29.36	0.42	0.97
ZK-153.8	75.60	59.40	14.70	56.70	10.80	2.46	12.34	1.94	12.10	2.88	7.11	0.89	4.41	0.57	98.50	261.90	34.20	0.41	0.98
ZK-154.1	18.70	14.70	3.16	12.90	2.52	0.54	2.65	0.41	2.83	0.75	2.03	0.31	2.06	0.28	26.40	63.83	35.44	0.43	0.97
ZK-154.6	111.00	89.90	24.50	102.00	20.10	4.61	21.35	3.28	20.10	4.63	11.70	1.49	7.19	1.02	138.00	422.86	29.81	0.40	1.03
ZK-155.3	89.60	70.30	19.10	80.40	15.50	3.91	16.66	2.74	15.30	3.65	9.35	1.08	5.44	0.71	113.00	333.74	30.96	0.39	1.13
ZK-155.8	52.20	40.30	10.20	43.80	8.21	2.06	8.44	1.26	7.65	1.78	4.40	0.56	2.67	0.37	63.50	183.90	35.67	0.40	1.15
Mean	**65.23**	**63.10**	**13.14**	**53.10**	**9.80**	**2.24**	**10.28**	**1.64**	**10.10**	**2.45**	**6.23**	**0.82**	**4.05**	**0.60**	**83.76**	**242.77**	**36.66**	**0.46**	**1.03**
δ	**33.78**	**28.42**	**8.16**	**34.68**	**6.70**	**1.53**	**7.32**	**1.13**	**6.94**	**1.63**	**4.04**	**0.46**	**1.99**	**0.28**	**47.67**	**182.72**	**5.75**	**0.12**	**0.20**
Samples	La	Ce	Pr	Nd	Sm	Eu	Gd	Tb	Dy	Ho	Er	Tm	Yb	Lu	Y	∑REE	Y/Ho	Ce/Ce*	Eu/Eu*
ZK-156.5	80.50	67.70	17.70	77.30	16.00	4.19	16.03	2.44	13.70	3.11	7.40	0.89	4.21	0.56	101.00	311.72	32.48	0.41	1.21
ZK-157.9	115.00	92.10	26.10	107.00	21.40	5.40	23.87	3.58	21.00	4.83	12.40	1.56	7.30	1.00	147.00	442.53	30.43	0.39	1.10
ZK-158.7	139.00	111.00	31.20	139.00	28.40	7.21	30.08	4.59	27.40	6.24	15.30	1.94	9.08	1.17	175.00	551.61	28.04	0.39	1.14
ZK-159.5	135.00	104.00	29.80	131.00	25.70	6.44	28.01	4.42	27.00	6.32	16.40	1.99	9.47	1.24	173.00	526.79	27.37	0.38	1.11
ZK-160	95.40	72.00	20.00	85.70	15.90	3.88	17.11	2.90	17.60	4.16	11.00	1.40	7.55	0.99	126.00	355.60	30.29	0.38	1.09
ZK-160.7	124.00	91.10	26.90	117.00	22.20	5.15	24.23	3.78	24.40	5.94	14.90	1.94	9.26	1.25	159.00	472.05	26.77	0.36	1.03
ZK-161.5	79.00	59.10	16.20	67.30	13.20	2.86	14.14	2.26	14.10	3.60	9.47	1.20	6.55	0.84	111.00	289.82	30.83	0.38	0.97
ZK-161.9	99.40	67.40	19.50	73.90	14.50	3.05	15.58	2.29	15.30	3.55	8.96	1.23	5.53	0.84	137.00	331.03	38.59	0.35	0.94
ZK-163.1	103.00	77.80	22.10	92.50	17.40	3.83	18.28	2.90	17.00	4.07	10.40	1.31	6.01	0.85	145.00	377.45	35.63	0.37	1.00
ZK-163.9	90.80	66.50	17.90	73.70	14.50	2.99	15.13	2.22	14.70	3.47	8.99	1.05	5.88	0.79	131.00	318.63	37.75	0.38	0.94
ZK-164.5	82.00	59.00	15.40	68.10	12.20	2.81	13.06	2.15	13.30	2.85	7.83	0.95	4.80	0.71	117.00	285.16	41.05	0.38	1.03
ZK-165.2	154.00	123.00	36.60	160.00	33.50	6.74	35.94	5.30	32.00	8.04	18.80	2.36	11.30	1.47	211.00	629.05	26.24	0.38	0.90
ZK-166.2	82.10	59.90	15.70	67.40	12.50	2.85	12.79	2.14	13.20	3.18	7.66	1.03	5.16	0.71	123.00	286.31	38.68	0.38	1.04
ZK-166.8	144.00	115.00	35.20	152.00	30.90	7.21	31.89	4.79	29.00	6.84	17.20	2.02	10.30	1.33	208.00	587.68	30.41	0.37	1.07
ZK-168.5	101.00	78.20	21.00	84.90	16.90	3.70	18.28	2.62	16.90	3.85	9.44	1.19	5.73	0.75	156.00	364.47	40.52	0.39	0.97
Mean	**108.28**	**82.92**	**23.42**	**99.79**	**19.68**	**4.55**	**20.96**	**3.22**	**19.77**	**4.67**	**11.74**	**1.47**	**7.21**	**0.97**	**148.00**	**408.66**	**33.01**	**0.38**	**1.04**
δ	**25.29**	**21.71**	**7.11**	**32.35**	**6.98**	**1.67**	**7.50**	**1.10**	**6.48**	**1.60**	**3.81**	**0.47**	**2.19**	**0.27**	**32.92**	**149.15**	**5.21**	**0.01**	**0.09**
ZK-168.9	3.83	4.46	0.62	2.42	0.38	0.09	0.44	0.08	0.52	0.12	0.33	0.06	0.34	0.05	5.76	19.50	48.81	0.65	1.05
ZK-169.1	4.43	5.11	0.71	2.65	0.48	0.12	0.50	0.09	0.57	0.15	0.39	0.05	0.37	0.05	6.20	21.87	41.33	0.65	1.15
ZK-170	8.84	10.70	1.57	5.95	1.04	0.23	0.97	0.16	0.85	0.20	0.50	0.07	0.31	0.05	10.30	41.74	52.82	0.65	1.06

Note: $Ce/Ce^* = 2Ce_N/(La_N + Nd_N)$, $Eu/Eu^* = 2Eu_N/(Sm_N + Gd_N)$ (Bau and Dulski, 1996).

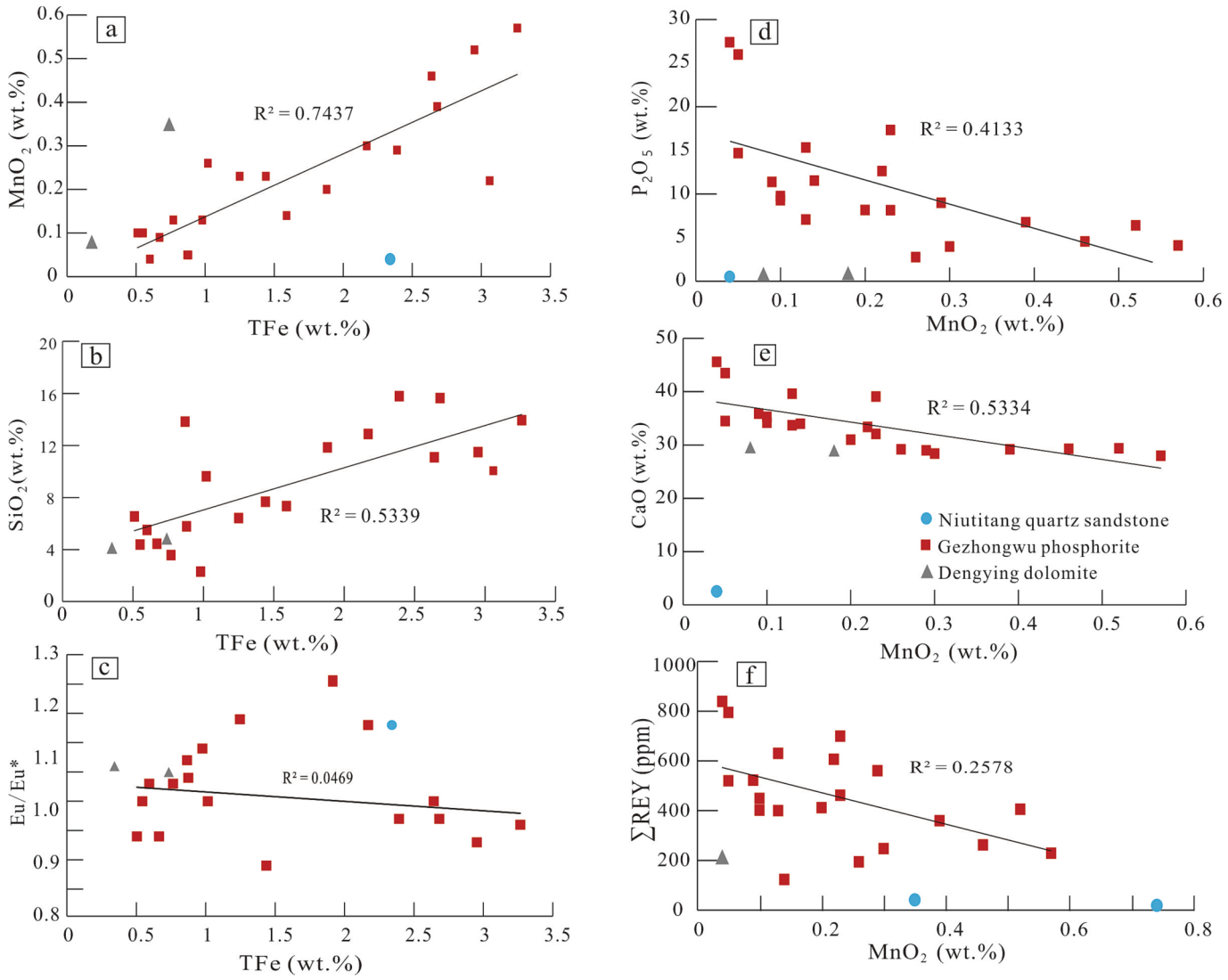

Fig. 3. Relationships between total Fe (TFe) and MnO_2 (a), SiO_2 (b), and Eu/Eu* (c) and relationships between MnO_2 and P_2O_5 (d), CaO (e), and ∑REE (f) of bulk phosphorite rocks from Zhijin deposit.

extraordinary REE enrichment in the Zhijin phosphorites. However, previous geochemical investigations were focused on bulk rocks, which is insufficient to understand the REE enrichment processes in francolites relative to Fe/Mn (oxyhydr)oxides.

Therefore, the bulk-rock geochemistry, the mineralogy, and in-situ geochemical features of Fe (oxyhydr)oxides from Zhijin phosphorite were studied to assess the roles of Fe/Mn (oxyhydr)oxides played in REE enrichment. Our findings implied that Fe (oxyhydr)oxides might originate from seawater, altered by late hydrothermal events. Fe (oxyhydr) oxides participated in REE enrichment in francolites via Fe redox cycling, in which Fe (oxyhydr)oxides adsorbed REEs in oxic water columns and released them into suboxic/anoxic porewater. After that, francolites formed and captured REEs during early diagenesis. This study provides new insights into Fe/Mn (oxyhydr)oxide participation in REE enrichment in marine phosphorites.

2. Geological setting

2.1. Paleogeography

During the Jinningian tectonics (900–820 Ma), the aggregation of Yangtze and Cathaysia Blocks occurred, forming the South China Plate and the Jiangnan Orogenic Belt (Shu, 2012; Zhang et al., 2013). After that, the ancient South China Plate underwent rifting and glaciation along with relatively stable tectonic movements (Shu, 2012). Until the late Neoproterozoic, the Yangtze Block and the Cathaysia Block broke up gradually along with the fragmentation of the Rodinia supercontinent (Wang and Li, 2003). In the early Cambrian, the South China Plate underwent steady supercontinent break-ups and maintained the same paleographic framework as the late Neoproterozoic (Liu et al., 1993). During the early Cambrian, South China was composed of shallow-water platform facies (Fig. 1a I), transitional facies (Fig. 1a II), and deep-water slope and basin facies (Fig. 1a III) from the northwest to southeast (Steiner et al., 2001). Shallow-water carbonate deposits dominated the platform facies and multiple phosphorite deposits formed such as Kunyang in Yunnan, Zhijin in Guizhou, and Hanyuan in Sichuan (Ye et al., 1989). Among them, the Zhijin phosphorite deposit contains enriched REEs and shows excellent potential as a REE resource.

2.2. Deposit geology

2.2.1. Ore bodies and sources

The Zhijin deposits are strata bound and spread northeast with cores of the Guohua-Gezhongwu Fault/Anticline (F_1/f_1) and Guiguo-Damachang Fault/Anticline (F_2/f_2) (Fig. 1b). The Zhijin phosphorite deposits are divided into the Xinhua Mining District on the northwestern

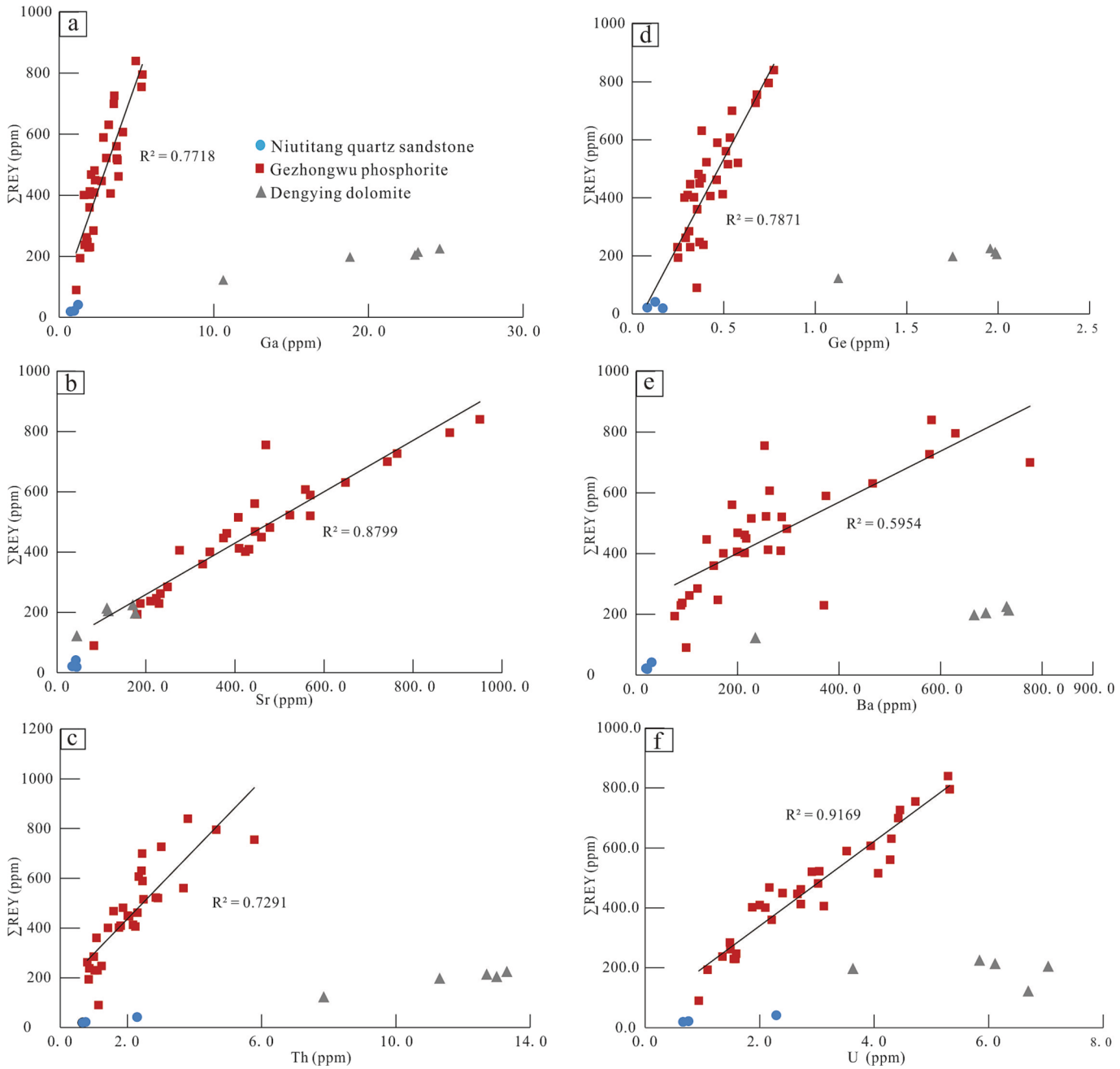

Fig. 4. Positive relationships between ∑REE and Ga (a), Sr (b), Th (c), Ge (d), Ba (e), and U (f) of bulk phosphorite rocks from the Zhijin deposit.

side and the Damachang Mining District on the southeastern side. The Xinhua Mining District includes the Daga, Motianchong, Guohua, Ganjiayakou, Gezhongwu, and Gaoshan ore blocks, which provide the most phosphate resources. The Zhijin deposit has phosphate mineral resources of ~ 3.39 billion tons and potential REE resources (RE_2O_3) of nearly 3.503 million tons, with P_2O_5 and RE_2O_3 grades of 17.20 % and 1036 g/t, respectively.

The P-bearing rock series was hosted in the Gezhongwu Formation, overlain by Niutitang sandy shale and underlain by Dengying dolomite. The thickness of the Gezhongwu Formation is ~ 20 m (Liu et al., 2020; Yang et al., 2021b), usually divided into the Lower and Upper Gezhongwu members. The Lower Gezhongwu comprises mainly dolomitic phosphorites and the Upper Gezhongwu comprises siliceous phosphorites. Biological fossils abound in the Zhijin deposit, including small shell fossils (SSF), macroscopic bacterial colonies, arthropods, sponges, and zooplankton (Wu et al., 1999; Mao and Yang, 2013).

2.2.2. *Isochron ages*

Early isotopic dating of early Cambrian phosphorites suggested the early Cambrian in South China started around 587 ± 17 Ma (Cowie and Johnson, 1985), 562 ± 5.7 Ma (Yang et al., 1996) using Rb-Sr and Sm-Nd isotopic compositions, respectively. Shi (2005) tested Sm-Nd/Rb-Sr isotope and suggested that Zhijin phosphorite formation started around 541 ± 12 Ma. Previous researchers suggested that the Niutitang black shales represented the Precambrian-Cambrian boundary. The isochron ages distract in ~ 560 ± 50 Ma (Horan et al., 1994), ~542 ± 11 Ma (Li et al., 2002), ~541 ± 16 Ma (Mao et al., 2002), and ~ 537 ± 10 Ma (Jiang et al., 2004). However, a subsequent Re-Os isotopic dating of Niutitang black shales (~521 Ma) claimed the sulfide ore layer did not mark the Precambrian-Cambrian transition but the upper limit of the Gezhongwu Formation (Xu et al., 2011). Therefore, early Cambrian Zhijin phosphorites likely formed earlier than 521 Ma, perhaps started around 541 Ma (Shi, 2005).

Table 4
Partial major and trace element correlations of early Cambrian phosphorite from the Zhijin deposit, Central Guizhou, South China.

	CaO	F	TFe_2O_3	MgO	MnO_2	P_2O_5	SiO_2	LOI	Be	Ga	Ge	Sr	Zr	Sb	Ba	Th	U	REY
CaO	1																	
F	**0.945****	1																
TFe_2O_3	−**0.659****	−**0.469***	1															
MgO	−**0.759****	−**0.920****	0.171	1														
MnO_2	−**0.730****	−**0.632****	**0.862****	0.401	1													
P_2O_5	**0.944****	**0.997****	−**0.472***	−**0.927****	−**0.643****	1												
SiO_2	−**0.706****	−**0.466***	**0.731****	0.112	**0.630****	−**0.453***	1											
SO_3	−0.294	−0.072	**0.728****	−0.190	**0.471***	−0.071	**0.575****											
LOI	−**0.774****	−**0.930****	0.191	**0.991****	**0.445***	−**0.937****	0.130	1										
Be	**0.532***	**0.552***	−0.184	−**0.519***	−0.299	**0.548***	−0.355	−**0.502***	1									
Ga	0.396	**0.526***	−0.094	−**0.481***	−0.333	**0.490***	−0.191	−**0.520***	**0.452****	1								
Ge	**0.485***	**0.640****	−0.141	−0.623**	−0.409	**0.613****	−0.132	−**0.660****	**0.446***	**0.930****	1							
Sr	**0.862****	**0.868****	−**0.458***	−**0.829****	−0.580**	**0.895****	−0.412	−**0.819****	**0.540****	0.207	0.344	1						
Zr	0.091	0.184	−0.016	−0.121	−0.179	0.140	−0.090	−0.161	0.169	**0.885****	**0.774****	−0.211	1					
Sb	0.244	0.303	−0.111	−0.303	−0.308	0.309	−0.022	−0.306	0.261	0.191	0.272	**0.373***	0.044	1				
Ba	**0.861****	**0.872****	−0.412	−**0.797****	−**0.486***	**0.875****	−**0.469***	−**0.786****	0.304	**0.354***	**0.462****	**0.833****	0.034	**0.367***	1			
Th	**0.454***	**0.577****	−0.222	−**0.521***	−**0.455***	**0.546***	−0.226	−**0.546***	**0.512****	**0.943****	**0.918****	0.287	**0.813****	0.309	**0.378***	1		
U	**0.650****	**0.769****	−0.173	−**0.740****	−0.438	**0.749****	−0.308	−**0.749****	**0.615****	**0.873****	**0.882****	**0.574****	**0.612****	**0.373***	**0.641****	**0.885****	1	
REY	**0.800****	**0.828****	−0.356	−**0.826****	−**0.508***	**0.855****	−0.370	−**0.804****	**0.656****	**0.395***	**0.394***	**0.944****	−0.147	**0.420***	**0.745****	**0.405***	**0.657****	1

Note: ** represents the significant correlation in 0.01 level; * represents the significant correlation in 0.05 level.

3. Sampling and methodologies

3.1. Samples

A total of 39 samples were sampled, which included 3 dolomite samples from the Dengying Formation, 15 dolomitic phosphorite samples from the Lower Gezhongwu, 17 siliceous dolomitic phosphorite samples from the Upper Gezhongwu, and 4 quartz siltstone samples from the Niutitang Formation. The near-pure phosphorites were defined by P_2O_5 levels > 15–18 % (Papineau, 2010), with P_2O_5 levels between 8 and 15 % defined as phosphatic rocks and < 8 % called P-bearing rocks. All Gezhongwu samples were named according to their P_2O_5 levels, which comprised mainly phosphorites and dolomitic phosphorites in the Lower Gezhongwu and siliceous dolomitic phosphorites and siliceous phosphatic dolomite in the Upper Gezhongwu (Table 1). Samples used for major and trace elemental analyses were ground into 200-mesh powders. For mineralogical and in-situ geochemical studies, phosphorite samples were cut to polished pieces that were 50-μm-thick and 100-μm-thick, respectively.

3.2. Methodologies

3.2.1. Major and trace element analyses of bulk rocks

The major elemental components of powder samples were analyzed at the ALS Minerals (Guangzhou) Co. Ltd. using X-ray fluorescence (XRF; ME-XRF24 for phosphorites, ME-XRF26 for carbonate rocks). Samples were digested using a $LiNO_3$ solution and wall rocks were digested by $Li_2B_4O_7$ and then melted at 1000 ℃. Another sample powder was burned at 1000 °C and subsequently weighted to obtain the loss on ignition (LOI). The detection limit for all major oxides was 0.01 wt%, with standard deviations < 1 % and errors < 3 %.

Trace elements were analyzed at the State Key Laboratory of Ore Deposit Geochemistry of the Institute of Geochemistry, Chinese Academy of Sciences (SKLODG-IGCAS), using a quadrupole inductively coupled plasma mass spectrometer (Q-ICP-MS), model ELAN-DRC-e ICP-MS (PerkinElmer, Inc., USA). Portions (50 mg) of the sample powders were digested using a solution of mixed HF and HNO_3. The analytical procedure and guidelines was based on Qi et al. (2000) and the internal standard was a 40 ng/mL Rh solution. The detection limits were as follows: Tb, Ho, Lu, and Tm (0.01 ppm); Er, Eu, Sm, Pr, and Yb (0.03 ppm); Ce, Gd, and Dy (0.05 ppm); Hf (0.2 ppm); Nd (0.1 ppm); Y and La (0.5 ppm); Zr and Mo (2 ppm). The relative standard deviations are generally better than 10 %.

3.2.2. Petrographic analyses of Fe/Mn (oxyhydr)oxides

The petrographic characteristics of Fe/Mn (oxyhydr)oxides were analyzed using a JSM-7800F field emission scanning electron microscope (SEM) (JOEL Ltd., Japan) at SKLODG-IGCAS. The sections and targets were coated with carbon to make the sections conductive. Under the SEM, backscattered electron (BSE) images were collected with a 10-kV, 4.5-nA electron beam, while energy dispersive spectrometer (EDS) analysis was conducted using a 10-kV, 4.5-nA electron beam. Fe/O ratios were calculated using EDS result based on the following equation:

$$Fe/O = [Fe] / ([O] - n * [X])$$

[Fe] represents the Fe percentage, [O] represents the O percentage, [X] represents the percentages of other metallic elements, n represents the relative atomic ratio of X oxides.

3.2.3. In-situ element analyses of Fe (oxyhydr)oxides

The in-situ major elements of Fe (oxyhydr)oxides were analyzed at the State Key Laboratory of Nuclear Resources and Environment, East China University of Technology using a JXA-8530F Plus electronic probe. The high-pressure beam emitted by the electric gun was accelerated under a 15-kV voltage and 10-mA current and bombarded the

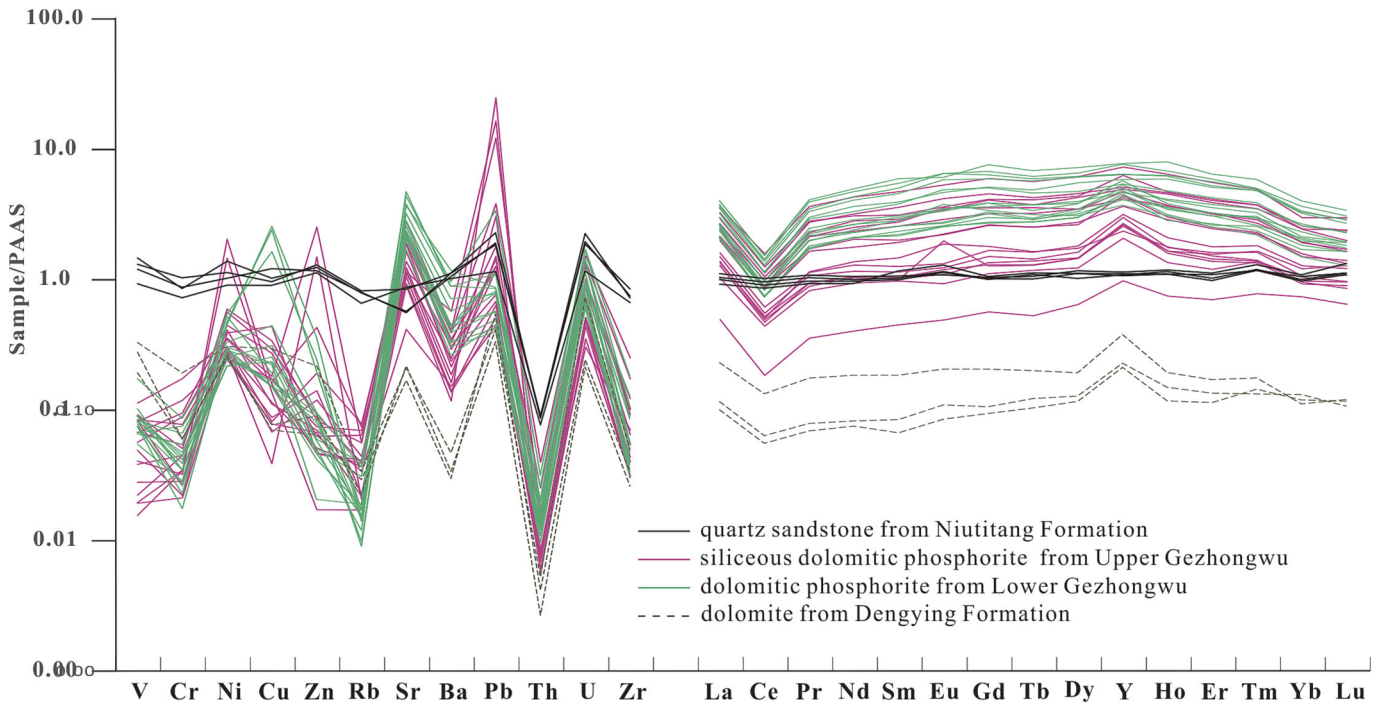

Fig. 5. PAAS-normalized REE distributions of bulk rocks from early Cambrian Zhijin phosphorites. PAAS data are from Taylor and McLennan (1985).

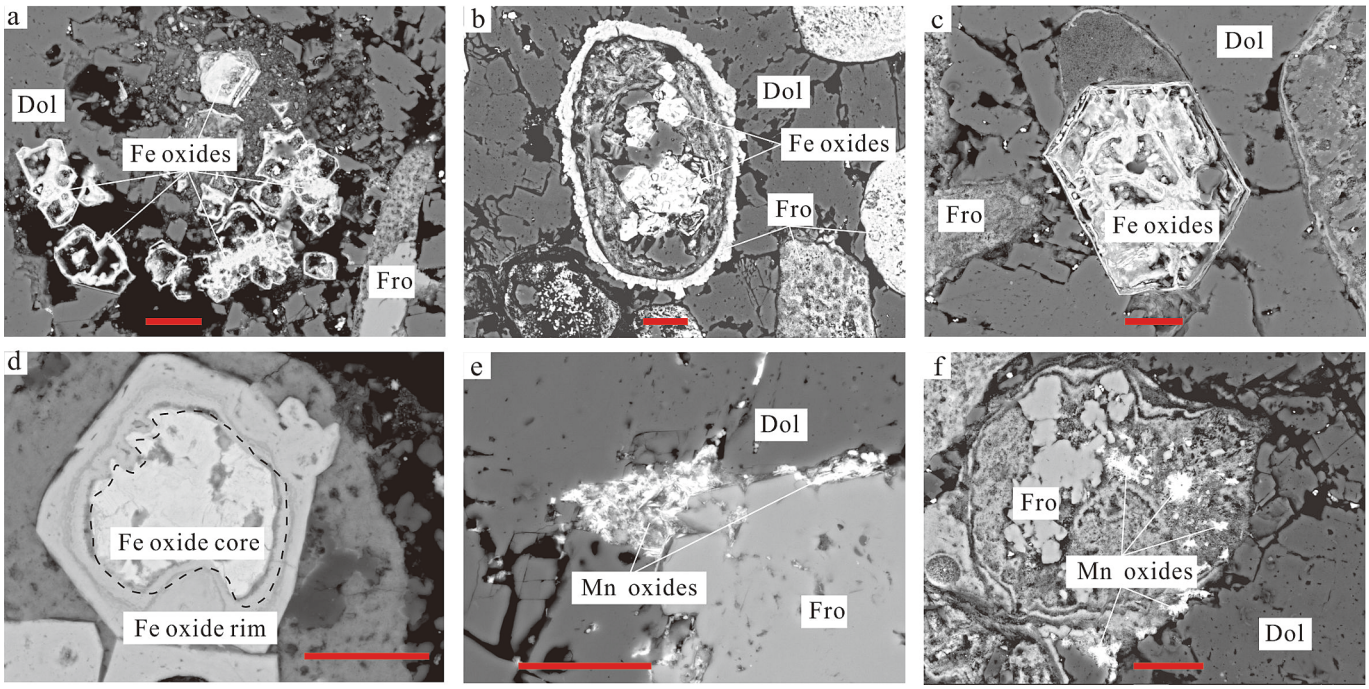

Fig. 6. Characteristics of Fe/Mn (oxyhydr)oxides from the Gezhongwu Formation, early Cambrian in Zhijin phosphorite, South China. (a) cubic Fe (oxyhydr)oxide particles were dispersed among the dolostones; (b) pelletiod Fe (oxyhydr)oxide hosted in authigenic phosphate grains; (c) six-party Fe (oxyhydr)oxide particles occurred in dolostones; (d) Fe (oxyhydr)oxides comprised a gray rim and a bright core; (e, f) flocculent Mn carbonates distributed dispersedly among the dolostones. Each red scale bar shown insert represents 20 μm. Abbreviation: Fro: francolite; Dol: dolomite.

mineral surface, exciting characteristic X-rays. Subsequently, the X-ray signals were collected for major element analyses. Magnetite and pyrite were used as standards for Fe (oxyhydr)oxides and Fe sulphides, respectively. The analytical error was less than 1 %, and the detection limit was < 0.01 %. Elemental mapping of Fe (oxyhydr)oxides was collected under a 15-kV voltage and 10-mA current.

The in-situ trace elements of Fe (oxyhydr)oxides were analyzed at SKLODG-IGCAS. The samples were ablated using a 44–60 μm laser mixed with an H_2/He carrier gas; the aerosol was sent into the ICP-MS for elemental signal collection. Every cyclicality of the signal collection contained a 30-s blank and a 50-s sample ablated signal; several standards (BIR-1G, BCR-2G, BC-28, GSE-1G) were examined before and after every ten samples. Elemental abundances were calculated by ICPMSDataCal (Liu et al., 2008) using multiple external standard

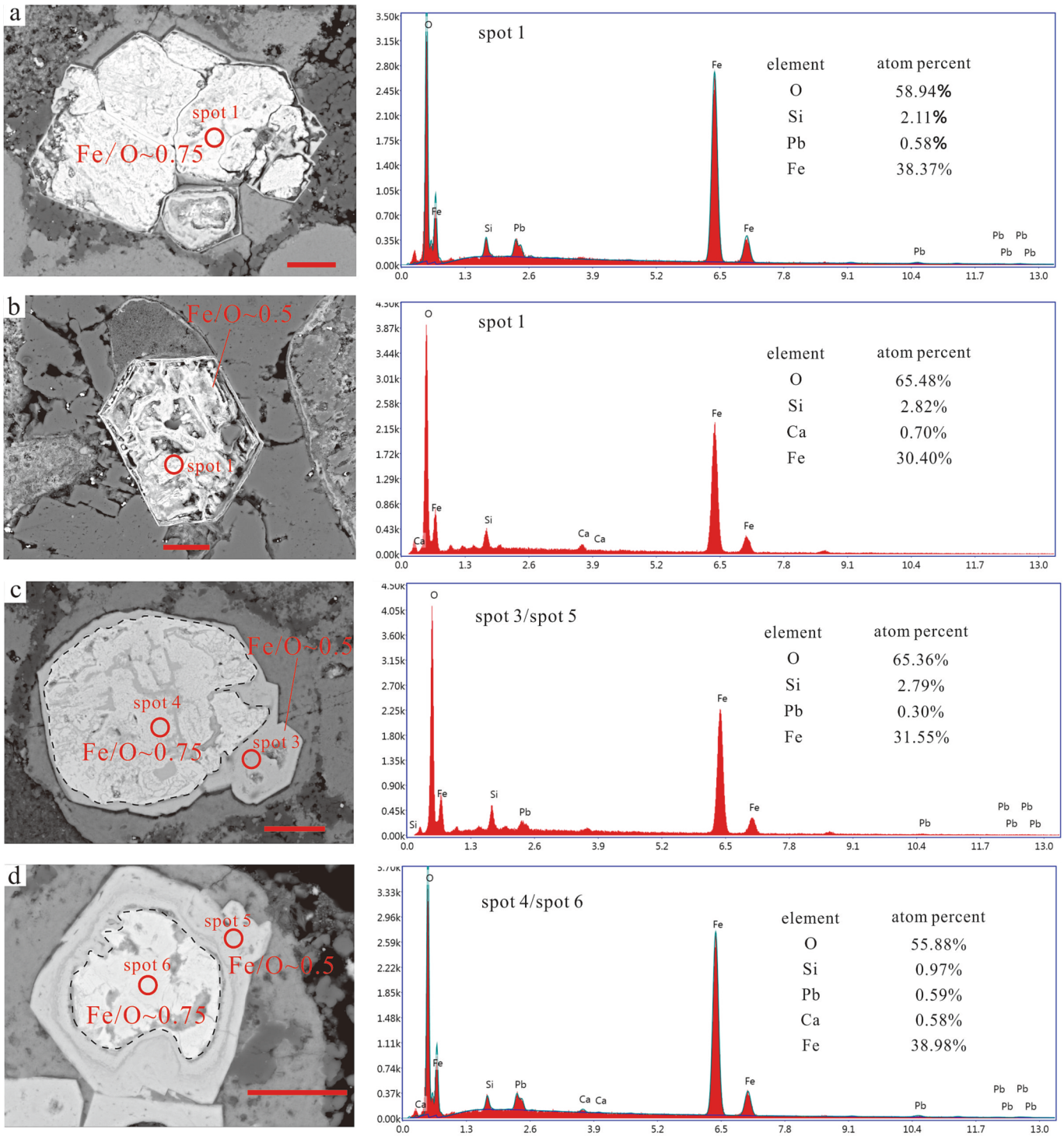

Fig. 7. SEM-EDS analyses of Fe (oxyhydr)oxides. Fe/O ratios were calculated using SEM-EDS results and the equation: Fe/O = [Fe] / ([O] – n * [X]), in which [Fe] represents the Fe percentage, [O] represents the O percentage, [X] represents the percentages of other metallic elements, and n represents the relative atomic ratios of X oxides.

methods, with BC-28 serving as the Fe (oxyhydr)oxide external standard. The detection limit was ppb-level and relative analytical errors did not exceed 10 %.

REE compositions were normalized to the Post Archean Australian shales (PAAS) (Taylor and McLennan, 1985). Ce and Eu anomalies were calculated using the following equations:

$Ce/Ce^* = 2Ce_N/(La_N + Nd_N)$; $Eu/Eu^* = 2Eu_N/(Sm_N + Gd_N)$ (Bau and Dulski, 1996)

Several in-situ elemental compositions of francolites in Zhijin phosphorites have been widely reported recently (Yang et al., 2021b; Zhang et al., 2021; Wu et al., 2022a; Yang et al., 2022a; Zhang et al., 2022). Here, the reported data were cited for comparison with the in-situ geochemical characteristics of Fe (oxyhydr)oxides. Mn (oxyhydr)oxides in Zhijin phosphorites were too small to investigate due to their flocculent textures.

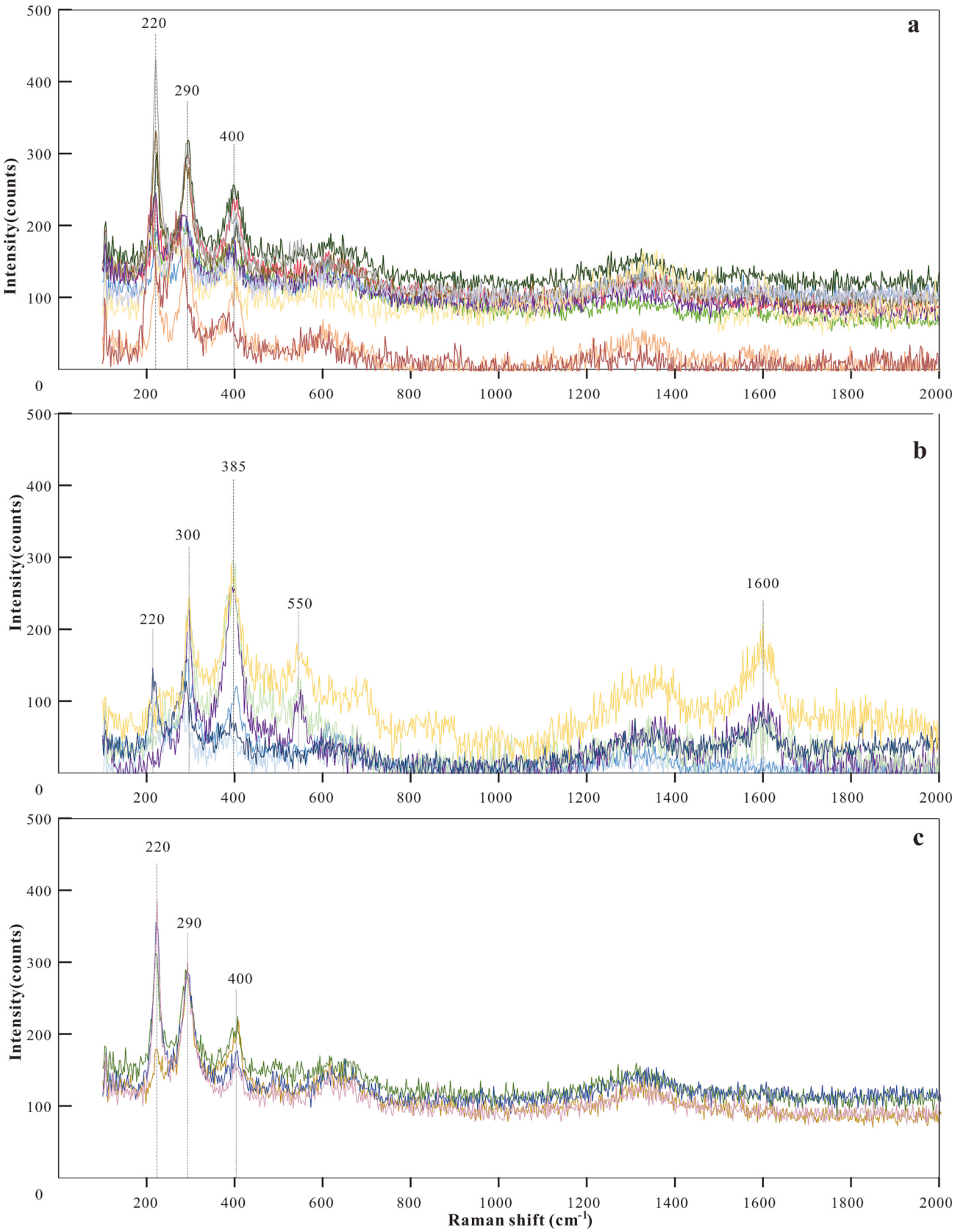

Fig. 8. Laser Raman spectral characteristics of the core (a) and rim (b) of Fe (oxyhydr)oxides and Fe (oxyhydr)oxide individual crystals (c).

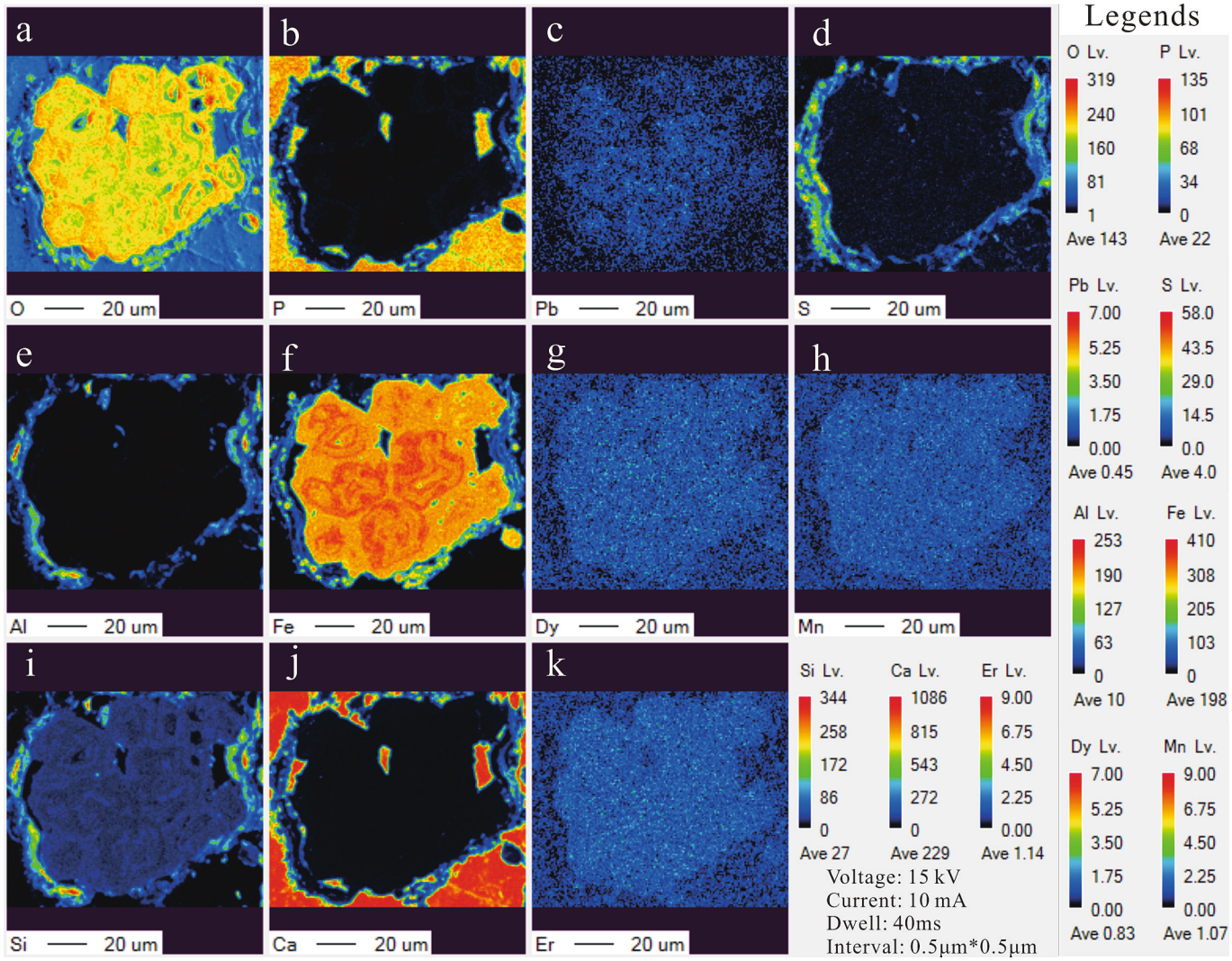

Fig. 9. Partial elemental mapping in Fe (oxyhydr)oxides from the Gezhongwu Formation.

3.2.4. Laser Raman analyses of Fe (oxyhydr)oxides

Laser Raman spectroscopic analyses of Fe (oxyhydr)oxides were conducted at SKLODG-IGCAS using a LabRAM HR Evolution Raman spectrometer with an argon ion laser (at 532 nm and 25 mW). The laser spot was ~ 2 μm in diameter. The energy of the argon ion laser was adjusted within the range of 10–30 % to ensure that iron was not oxidized. The Raman spectra were acquired from 100 to 2000 cm^{-1} with acquisition times between 30 and 60 s for each analysis.

4. Results and discussion

4.1. Mineralogical and geochemical characteristics of bulk phosphorite and francolites: Diagenetic enrichment

The phosphorite hand specimens are mainly massive (Fig. 2a) and banded (Fig. 2b, c). Mineral compositions primarily comprise phosphate minerals and gangue minerals which include dolomite, calcite, quartz, magnetite, K-feldspar, muscovite, and Fe/Mn oxides (detailed in Yang et al. (2021b)). Our previous study identified three types of phosphate minerals in Zhijin phosphorite: biodetritus (Fig. 2d), abiogenic grains (Fig. 2e), and apatite individuals (Fig. 2f). Among them, apatite individuals were divided into authigenic/diagenetic francolites, terrigenous clastic apatites, and hydrothermally altered apatites (Yang et al., 2022b). Detailed descriptions have been published previously (Yang et al., 2021a; Yang et al., 2021b; Yang et al., 2022b). Tables 1–3 list the major and trace elements of bulk rocks from the Zhijin profile. The Lower Gezhongwu had lower levels of Al_2O_3 (mean of 0.47 %), total Fe (TFe, 0.90 %), MgO (11.72 %), SiO_2 (6.47 %), and LOI (27.06 %) and higher CaO (37.24 %), F (1.56 %), P_2O_5 (14.66 %) than the Upper Gezhongwu (mean levels of 1.03 %, 2.32 %, 14.02 %, 14.56 %, 31.88 %, 30.20 %, 0.85 %, and 7.01 %, respectively). Total Fe has correlated positively with MnO_2, SiO_2, and SO_3 (Table 3, Fig. 3a-c) while relates negatively to P_2O_5, CaO, F, Sr, and Ba in bulk rocks (Table 3, Fig. 3d-f). This might imply an isogenesis and symbiotic relationship of Fe and Mn (oxyhydr)oxides (Prakash, 2012).

The ∑REE of bulk rocks from the Lower Gezhongwu (average = 556.66 ppm) is much higher than those of Upper Gezhongwu (average = 326.52 ppm). ∑REE relates closely to collophane concentrations as REE elements congregate in francolites via isomorphous substitution (Nie, 2018; Yang et al., 2021b). ∑REE correlated positively with Ga (Fig. 4a), Sr (Fig. 4b), Th (Fig. 4c), Ge (Fig. 4d), Ba (Fig. 4e), and U (Fig. 4f). Furthermore, more correlationships between major and trace elements were listed in Table 4. Fig. 5 displays the post-Archean Australian shale (PAAS)-normalized trace element distributions of Dengying dolomites, Gezhongwu phosphorites, and Niutitang quartz siltstones. Compared with PAAS, partial phosphorite rich in Sr, Pb, and U, while the PAAS-normalized distributions of dolomites and quartz siltstones showed flat REE plots. Gezhongwu phosphorite samples have "hat-shaped" REE plots, characterized by enrichment of MREEs as compared to LREEs and HREEs. Previously, MREE-enriched to bell-

Table 5
In-situ major element compositions of Fe (oxyhydr)oxides from the Zhijin deposit, South China.

No.	MgO	Al_2O_3	SiO_2	P_2O_5	PbO	CaO	TiO_2	FeO	MnO	BaO	SO_3	Total
ZK-160.7-1′	1.24	1.17	4.51	0.38	0.08	0.37	0.03	68.41	0.08	–	0.04	76.30
ZK-160.7-2′	0.52	0.10	4.15	0.19	0.09	0.35	–	71.37	0.02	0.01	0.01	76.81
ZK-160.7-3′	0.53	0.10	3.64	0.12	0.02	0.42	–	72.31	–	0.01	0.04	77.19
ZK-160.7-4	0.48	0.05	3.21	0.06	0.03	0.25	–	71.93	–	0.00	0.03	76.04
ZK-160.7-5	0.52	0.07	3.33	0.08	0.04	0.59	–	72.07	0.03	0.00	0.02	76.75
ZK-160.7-6′	0.54	0.07	3.70	0.12	0.08	0.31	–	72.85	0.07	–	0.05	77.79
ZK-160.7-7	0.23	0.08	2.95	0.09	0.16	0.52	0.01	78.64	0.04	0.01	0.09	82.82
ZK-160.7-8′	0.49	0.10	3.39	0.18	0.13	0.55	–	72.64	0.04	–	0.05	77.55
ZK-160.7-9′	0.41	0.05	3.35	0.09	0.12	0.29	–	72.15	0.03	–	0.04	76.52
ZK-160.7-10	0.59	0.13	4.16	0.29	0.09	0.33	0.00	73.16	0.02	–	0.05	78.81
ZK-160.7-11	0.51	0.05	3.34	0.06	0.01	0.24	0.00	74.35	0.04	–	0.02	78.63
ZK-159.5-1	1.46	0.02	3.78	0.27	0.08	0.57	0.02	75.50	0.09	–	0.17	81.95
ZK-159.5-2′	0.22	0.01	2.88	0.21	0.54	0.49	–	82.84	0.03	0.01	0.14	87.37
ZK-159.5-3	1.20	0.03	3.54	0.60	0.08	0.44	–	73.34	0.07	0.02	0.12	79.43
ZK-159.5-4′	0.19	0.04	2.54	0.22	0.66	0.46	0.00	82.27	0.02	0.03	0.13	86.55
ZK-159.5-5′	1.19	0.34	2.67	0.91	0.09	1.49	0.03	70.72	0.03	–	0.09	77.56
ZK-159.5-6	0.89	0.16	3.41	0.52	0.15	0.74	0.06	66.14	0.09	0.02	0.12	72.30
ZK-159.5-7	1.16	0.09	3.07	0.91	0.12	0.99	–	69.54	0.05	0.01	0.07	76.01
ZK-159.5-8′	1.45	0.16	3.45	0.59	0.18	1.21	–	70.49	0.08	0.03	0.12	77.77
ZK-159.5-9	1.36	0.14	3.56	0.70	0.12	1.24	–	70.84	0.08	–	0.12	78.16
ZK-159.5-10	1.22	0.18	3.14	0.72	0.23	1.24	0.02	69.09	0.04	–	0.10	75.99
ZK-159.5-11	0.58	0.09	2.75	0.86	0.18	0.85	–	68.97	0.04	0.00	0.06	74.38
ZK-155.8-1	0.44	0.20	2.61	2.27	0.14	2.43	0.11	67.32	0.02	0.02	0.04	75.59
ZK-155.8-2′	0.47	0.05	3.11	0.15	0.04	0.76	–	78.94	0.06	–	0.07	83.66
ZK-155.8-3	0.30	0.05	3.08	0.11	0.13	0.86	–	81.25	0.13	0.04	0.06	86.01
ZK-155.8-4	0.82	0.29	5.07	0.11	0.04	0.99	–	72.85	0.08	0.02	0.07	80.34
ZK-155.8-5′	1.31	0.64	5.39	0.09	0.01	0.83	–	81.23	0.03	0.02	0.03	89.57
ZK-151.9-1′	0.61	0.27	3.08	1.01	0.17	1.65	0.03	74.33	0.02	0.02	0.13	81.32
ZK-151.9-2′	0.23	0.01	3.35	0.10	0.23	1.41	–	79.90	0.01	0.02	0.09	85.35
ZK-151.9-3	0.38	0.13	2.81	0.36	0.17	7.82	–	68.94	0.04	0.03	0.29	80.96
ZK-151.9-4	0.45	0.02	3.02	0.45	0.10	2.83	–	74.58	0.01	0.02	0.07	81.54
ZK-151.9-5	0.74	0.02	3.41	0.60	0.21	0.57	0.09	70.71	0.09	–	0.13	76.58
ZK-151.9-6′	1.34	0.03	3.64	0.29	0.12	0.53	0.01	72.77	0.11	0.02	0.19	79.04
ZK-151.9-7′	0.24	0.00	2.63	0.23	0.67	0.41	0.01	81.92	0.06	0.04	0.13	86.33
Mean	**0.71**	**0.14**	**3.40**	**0.41**	**0.16**	**1.03**	**0.03**	**73.66**	**0.05**	**0.02**	**0.09**	**79.67**
Max	1.46	1.17	5.39	2.27	0.67	7.82	0.11	82.84	0.13	0.04	0.29	89.57
Min	0.19	0.00	2.54	0.06	0.01	0.24	0.00	66.14	0.01	0.00	0.01	72.30
δ	**0.71**	**0.14**	**3.40**	**0.41**	**0.16**	**1.03**	**0.03**	**73.66**	**0.05**	**0.02**	**0.09**	**79.67**
Mean in exterior	**0.68**	**0.20**	**3.47**	**0.31**	**0.20**	**0.72**	**0.02**	**75.32**	**0.05**	**0.02**	**0.08**	**81.04**
Mean in interior	**0.74**	**0.10**	**3.35**	**0.50**	**0.12**	**1.30**	**0.04**	**72.18**	**0.06**	**0.02**	**0.09**	**78.46**

Note: Unites for all elements are wt.%.
Numbers with superscript comma represent exterior of the Fe (oxyhydr)oxides, while others represent interior of the Fe (oxyhydr)oxides.

shaped patterns in phosphorite were deemed to represent secondary signatures rather than primary information in seawater, attributed to MREE were absorbed from pore water during diagenesis (Felitsyn and Morad, 2002; Kidder et al., 2003; Emsbo et al., 2015; Yang et al., 2022a). The REE geochemical indexes in Zhijin phosphorites, including positive relationships between Ce anomalies and ∑REE and negative relationships with Dy_N/Sm_N and Eu anomalies, supported diagenetic alteration (Liu, 1989; Yang et al., 2021b).

In addition, recent/modern sedimentary francolites might serve as the predecessors of old francolites during long-term burial and diagenetic processes, during which REE compositions were modified (Yang et al., 2022a). Therefore, we infer that francolites in Zhijin phosphorites formed during early diagenesis (Yang et al., 2021a; Wu et al., 2022a). All biodetritus, abiogenic grains, and authigenic/diagenetic francolite individuals formed in porewater related to early diagenesis. Whereas, terrigenous apatite individuals and hydrothermally altered apatites might be irrelevant with diagenesis (Yang et al., 2021a; Yang et al., 2021b; Yang et al., 2022b). Recent research distinguished carbonate-fluorapatite and carbon-free fluorapatite in Zhijin phosphorites according to XRD analyses, which indicated that francolites endured diagenesis and transformation (Yang et al., 2021b), in which carbonate-fluorapatite readily recrystallized and expelled CO_2 to form carbon-free fluorapatite eventually (Liu, 1989; Yang et al., 2021b).

REE uptake of francolites took place during diagenesis involves two perspectives. On one hand, authigenic/diagenetic francolite individuals have larger diameters. Previous research showed that both biodetritus and abiogenic grains were composed of nano-μm-scale francolites (Liu and Zhou, 2017; Xing et al., 2021). Whereas, authigenic/diagenetic francolite individuals have diameters between 50 and 100 μm, which implied their growth during diagenesis. On the other hand, authigenic/diagenetic francolite individuals have higher ∑REE, Ce/Ce*, and Eu/Eu* ratios than biodetritus and abiogenic grains (Yang et al., 2021a). These also indicated stronger diagenesis of authigenic/diagenetic francolite individuals than nano-scale apatite (Yang et al., 2021b; Yang et al., 2022b). Mineralogical characteristics of francolites confirm that francolites underwent diagenetic formation, which provided the opportunity for francolites to enrich REEs. During this process, francolites grew up alongside stronger diagenesis and absorbed REEs from porewater, resulting in higher REE concentrations in authigenic/diagenetic francolite individuals than nano-scale apatites in collophanites (Yang et al., 2022b).

4.2. *Mineralogical characteristics of the Fe/Mn (oxyhydr)oxide: Fe (oxyhydr)oxide formation*

The mineralogical characteristics of Fe/Mn oxides were investigated using SEM (Fig. 6). Most Fe oxides have cubic (Fig. 6a), pelletiod (Fig. 6b), and six-party (Fig. 6c) textures with diameters between 10 and

Table 6
In-situ trace elemental compositions of Fe (oxyhydr)oxides and mean values of francolites from Zhijin deposit, South China.

No.		V	Ni	Sr	Y	Ba	Pb	
Influenced by francolites		1	23.87	31.73	65.99	41.24	45.10	24089.10
		2	66.99	79.03	262.08	162.05	147.00	16712.68
		3	32.28	40.32	326.64	216.98	168.54	14021.21
		4	30.45	52.48	208.02	131.68	84.04	18509.57
		5	48.36	51.66	137.33	83.93	65.06	20425.99
		6	32.33	48.67	36.58	22.56	46.84	24302.80
		7	24.84	28.43	376.93	253.21	178.56	15070.59
		8	55.77	49.63	168.21	102.68	120.12	16075.82
		9	38.25	41.52	19.54	10.85	30.30	26272.78
		10	81.02	112.62	81.07	58.30	59.67	19464.71
		11	51.26	22.31	87.59	42.31	49.54	1463.63
		12	103.43	106.08	47.32	35.34	47.07	22266.88
		Mean	**49.07**	**55.37**	**151.44**	**96.76**	**86.82**	**18222.98**
Type 1		1	74.68	111.42	16.07	14.05	28.65	22281.35
		2	39.29	26.76	15.52	7.63	23.09	28166.22
		3	40.76	49.67	7.46	5.24	14.35	16857.44
		4	87.09	96.98	11.66	9.82	25.86	22860.87
		5	45.50	81.00	23.02	4.35	36.28	1404.97
		6	39.12	80.96	20.60	3.89	23.69	1230.55
		7	61.88	76.89	23.53	2.55	32.27	1556.49
		8	58.47	53.67	32.41	2.27	49.97	1796.44
		Mean	**55.85**	**72.17**	**18.78**	**6.23**	**29.27**	**12019.29**
Type 2		1		94.20	26.29	8.31	41.08	1602.15
		2		66.82	25.40	3.18	32.94	1923.97
		3		110.91	26.59	7.01	33.73	1068.22
		4		77.24	42.74	7.48	33.96	1202.92
		5		102.59	21.27	8.75	29.37	1347.11
		6		38.67	37.96	5.11	56.92	2138.46
		7		37.76	21.32	3.66	29.10	1741.61
		8		101.46	18.49	3.01	26.55	1240.79
		9		127.95	12.89	5.29	20.46	709.93
		10		78.29	40.29	9.38	79.15	2348.09
		Mean		**83.59**	**27.32**	**6.12**	**38.33**	**1532.33**
francolites		Max	46.08	7.42	1432.49	282.18	783.57	827.67
		Min	0.22	–	706.85	578.89	19.40	0.57
		Mean	**2.70**	**1.12**	**1061.13**	**839.59**	**352.55**	**77.68**
		δ	6.26	1.33	149.23	107.22	154.36	136.70

Samples		La	Ce	Pr	Nd	Sm	Eu	Gd	Tb	Dy	Ho	Er	Tm	Yb	Lu	∑REE	Y/Ho	Ce/Ce*	Eu/Eu*	
Influenced by francolites		1	24.51	15.59	3.52	14.98	2.53	0.61	3.62	0.45	3.15	0.69	2.01	0.24	1.29	0.16	114.60	59.39	0.35	0.91
		2	100.29	68.60	15.31	67.70	11.84	2.77	15.13	1.92	12.56	2.90	8.38	0.98	5.74	0.75	476.91	55.89	0.36	0.94
		3	139.66	95.52	20.96	89.02	16.01	3.74	19.47	2.42	17.03	3.69	10.75	1.16	6.04	0.74	643.20	58.74	0.37	0.97
		4	81.52	56.20	12.55	54.14	9.54	2.31	12.02	1.57	10.29	2.31	6.50	0.73	4.10	0.46	385.91	57.11	0.37	0.99
		5	52.26	36.21	8.23	35.92	6.46	1.53	7.78	1.00	6.97	1.44	4.17	0.47	2.59	0.30	249.27	58.08	0.36	0.99
		6	11.67	9.17	2.16	9.02	1.65	0.39	2.05	0.26	1.85	0.39	1.08	0.13	0.72	0.10	63.18	57.22	0.39	0.97
		7	158.17	104.57	23.63	100.05	17.59	4.13	21.48	2.81	19.96	4.39	12.71	1.34	7.33	0.88	732.27	57.63	0.36	0.97
		8	63.45	43.08	9.49	39.87	7.09	1.67	8.82	1.12	7.69	1.73	5.39	0.63	3.76	0.50	296.98	59.50	0.37	0.96
		9	5.87	3.80	0.82	3.66	0.63	0.17	0.82	0.12	0.81	0.20	0.57	0.07	0.44	0.06	28.90	55.25	0.35	1.08
		10	29.83	22.98	5.19	21.78	4.05	0.99	7.75	0.67	4.55	1.01	2.99	0.39	2.35	0.31	163.15	57.96	0.39	0.76
		11	24.63	19.55	3.80	17.69	3.44	0.71	3.63	0.49	3.36	0.73	1.97	0.25	1.40	0.20	124.14	58.33	0.41	0.93
		12	15.69	10.61	2.13	9.38	1.68	0.48	2.32	0.31	2.54	0.63	2.11	0.30	2.59	0.27	86.38	56.10	0.38	1.09
		Mean	**58.96**	**40.49**	**8.98**	**38.60**	**6.88**	**1.63**	**8.74**	**1.09**	**7.56**	**1.68**	**4.89**	**0.56**	**3.19**	**0.39**	**270.87**	**57.60**	**0.36**	**0.92**
type 1		1	3.52	2.35	0.48	2.07	0.41	0.11	0.56	0.09	0.78	0.25	1.02	0.17	1.59	0.21	27.68	55.23	0.37	1.02
		2	3.62	2.33	0.50	2.29	0.42	0.09	0.60	0.07	0.55	0.13	0.43	0.07	0.39	0.05	19.18	57.05	0.35	0.82
		3	1.47	0.94	0.18	0.76	0.12	0.03	0.29	0.03	0.34	0.09	0.38	0.07	0.52	0.08	10.54	58.07	0.38	0.76
		4	1.60	0.91	0.18	0.68	0.21	0.06	0.35	0.04	0.52	0.17	0.67	0.12	0.92	0.15	16.41	56.56	0.36	0.94
		5	2.08	3.02	0.19	0.80	0.14	0.05	0.22	0.04	0.38	0.10	0.46	0.08	0.89	0.14	12.94	43.68	0.95	1.26
		6	1.88	2.11	0.23	1.10	0.16	0.04	0.29	0.03	0.29	0.08	0.32	0.05	0.64	0.10	11.21	49.04	0.63	0.81
		7	1.01	0.46	0.08	0.38	0.06	0.02	0.14	0.02	0.15	0.04	0.21	0.04	0.60	0.09	5.84	71.19	0.30	0.72
		8	0.56	0.24	0.05	0.30	0.03	0.01	0.11	0.01	0.07	0.04	0.17	0.03	0.31	0.06	4.27	63.17	0.25	0.76
		Mean	**1.97**	**1.54**	**0.24**	**1.05**	**0.19**	**0.05**	**0.32**	**0.04**	**0.39**	**0.11**	**0.46**	**0.08**	**0.73**	**0.11**	**13.51**	**56.75**	**0.45**	**0.88**

samples	La	Ce	Pr	Nd	Sm	Eu	Gd	Tb	Dy	Ho	Er	Tm	Yb	Lu	∑REE	Y/Ho	Ce/Ce*	Eu/Eu*	
type 2	1	2.28	4.85	0.22	1.13	0.15	0.06	0.34	0.05	0.50	0.20	1.18	0.17	2.26	0.35	22.06	41.92	1.27	1.19
	2	1.48	4.40	0.11	0.58	0.09	0.03	0.04	0.01	0.22	0.05	0.25	0.04	0.61	0.09	11.19	65.10	1.92	2.17
	3	1.89	5.42	0.21	0.72	0.11	0.05	0.19	0.05	0.45	0.17	0.66	0.17	1.76	0.21	19.06	42.37	1.88	1.61
	4	5.04	10.12	0.71	0.91	0.12	0.09	1.03	0.07	0.55	0.28	0.78	0.18	1.69	0.26	29.31	26.92	1.57	0.65
	5	2.99	11.65	0.70	3.34	0.72	0.09	1.07	0.12	1.11	0.23	0.95	0.16	1.35	0.26	33.48	37.90	1.59	0.45
	6	2.86	11.73	0.23	0.73	0.17	0.06	0.22	0.05	0.34	0.12	0.34	0.07	0.94	0.13	23.09	43.04	2.99	1.45

(*continued on next page*)

Table 6 (*continued*)

samples	La	Ce	Pr	Nd	Sm	Eu	Gd	Tb	Dy	Ho	Er	Tm	Yb	Lu	∑REE	Y/Ho	Ce/Ce*	Eu/Eu*	
	7	1.44	2.38	0.14	0.64	0.08	0.04	0.12	0.02	0.22	0.08	0.30	0.05	0.61	0.08	9.84	46.38	1.03	1.72
	8	0.95	3.18	0.08	0.34	0.09	0.02	0.08	0.02	0.12	0.05	0.28	0.06	0.73	0.11	9.10	61.72	2.23	0.98
	9	0.96	7.51	0.08	0.24	0.04	0.04	0.19	0.02	0.23	0.07	0.45	0.12	1.27	0.22	16.74	74.23	5.69	1.49
	10	4.05	25.10	0.58	2.71	0.38	0.08	0.70	0.11	0.85	0.18	0.96	0.16	1.46	0.24	46.95	52.23	3.28	0.69
Mean		**2.39**	**8.63**	**0.31**	**1.13**	**0.20**	**0.06**	**0.40**	**0.05**	**0.46**	**0.14**	**0.61**	**0.12**	**1.27**	**0.19**	**22.08**	**49.18**	**2.35**	**1.24**	
francolite	Max	137.84	109.92	34.61	160.11	28.61	6.12	35.04	4.76	30.53	6.32	13.41	1.31	5.16	0.53	662.83	47.20	0.27	0.88
	Min	403.41	230.33	60.07	271.86	49.59	11.34	60.04	8.14	50.28	10.91	27.03	3.04	14.93	1.78	1202.77	53.76	0.30	0.95
	Mean	**573.10**	**404.08**	**100.47**	**461.90**	**88.34**	**19.97**	**104.89**	**14.17**	**86.00**	**17.89**	**42.82**	**4.52**	**20.71**	**2.49**	**1926.14**	**57.73**	**0.35**	**1.32**	
	δ	95.39	62.14	12.47	55.73	10.68	2.59	12.50	1.69	10.41	2.23	5.41	0.59	2.84	0.35	257.30	1.89	0.03	0.07	

Note: Unites for Na_2O, Al_2O_3, SiO_2, P_2O_5, K_2O, CaO, and FeO are wt.%, whereas for other elements are ppm. The mean values of francolites are from our previous study (Yang et al., 2021).

50 μm. The majority of Fe oxides had gray rim and a bright core (Fig. 6d), while a small number of Fe oxides showed individual crystals (Fig. 6c). Mn oxides have flocculent textures, with diameters between 5 and 20 μm (Fig. 6e, f). Two symbiotic relationships were observed: (1) Fe/Mn oxides occur in a dispersed fashion among francolites and dolostones (Fig. 6a, c), even cemented by dolomite (Fig. 6e); (2) Fe/Mn oxides occur within authigenic phosphate grains (Fig. 6b, d, f).

SEM-EDS analyses of Fe/Mn oxides are detailed in Supplement-A. We calculated the Fe/O ratios based on Eq. 1 to distinguish Fe/Mn (oxyhydr)oxide types, with EDS providing elemental percentages. Four groups of Fe/O ratios are distinguished: (1) ranging from 0.70 to 0.72; (2) ranging from 0.62 to 0.68; (3) ranging from 0.42 to 0.59; and (4) 0.31–0.38 (Fig. 7) (Supplement-A-Table 1). There are generally three Fe oxides, including FeO, Fe_2O_3, and a mixture (Fe_3O_4), and two kinds of Fe (oxyhydr)oxides, $Fe(OH)_2$ and $Fe(OH)_3$. In the nature, FeO readily oxidizes into Fe_2O_3 or Fe_3O_4, forming hematite/limonite or magnetite, respectively. In addition, Fe (oxyhydr)oxides are naturally unstable and readily transform into goethite via oxidation and/or weathering. This occurs in magnetite and/or hematite as well.

Fe (oxyhydr)oxide types were distinguished ignoring other negligible elements under EDS. In our samples, Fe (oxyhydr)oxides with Fe/O ratios of ~ 0.60–0.68 and 0.70–0.72 were identified as hematite/limonite and magnetite. Furthermore, Fe (oxyhydr)oxides with Fe/O ratios of ~ 0.5 and 0.33 (Supplement-A-Table 1) were identified as H_2O-bearing Fe oxides (such as goethite). Characteristics of the minerals implied that Fe (oxyhydr)oxides changed during oxidation and/or weathering processes. SEM and EDS analysis revealed that the individual crystals had Fe/O ratios between 0.74 and 0.53, with incompact textures (Fig. 7a, b). Besides, numerous Fe (oxyhydr)oxides consisted of a gray rim and a bright core (Fig. 2f, g) and showed a Fe/O ratio of ~ 0.70 at the core and ~ 0.53 at the rim (Fig. 7c, d). This implied gradual oxidization of Fe (oxyhydr)oxides rim.

As EDS could only yielded qualitative data, Fe (oxyhydr)oxide types require additional evidence, such as laser Raman. In this study, laser Raman showed different spectral characteristics in the core and rim of Fe (oxyhydr)oxides. In the Fe (oxyhydr)oxide core, vibration bands (peak values) were observed at 220, 290, and 400 cm^{-1} (Fig. 8a), which corresponded with hematite (Frezzotti et al., 2012). Vibration bands of the Fe (oxyhydr)oxide rim were 385, 300, 550, 220, and 1600 cm^{-1} (Fig. 8b), consistent with goethite (Hurai et al., 2015). In contrast, vibration bands of the Fe (oxyhydr)oxide individuals were observed at 220, 290, and 400 cm^{-1} (Fig. 8c), consistent with Fe (oxyhydr)oxide core (hematite) (Fig. 8a) (Frezzotti et al., 2012). This indicated that hematite transforms into goethite from the surface to the core during oxidation and/or weathering. Elemental mapping collected via EPMA showed the relative O levels increased from the core to the rim (Fig. 9a), while relative Fe levels showed an opposite trend (Fig. 9f). This supports a gradual oxidation from hematite to goethite. Therefore, we inferred that external goethite was the product of weathering/ oxidation, while internal hematite and hematite individuals might record the information of Fe (oxyhydr)oxide precipitation and diagenesis. This may provide evidence for REE transformation and enrichment in phosphorite (discussed below).

Partial elemental mapping (full details in supplement-B) showed Fe (oxyhydr)oxides are enriched in partial REEs, including Nd, Tb, Dy, Er, and Tm, but not Y. Mn (oxyhydr)oxides appeared consistently with Fe oxides, rich in S, Ce, Eu, Gd, Dy, and Tb, while collophane showed lower REE levels than Fe/Mn (oxyhydr)oxides. This disagreed with later LA-ICP-MS results (detailed in section 4.3). This might be attributed to the false peaks of REEs due to their similar characteristic X-ray patterns with Fe and/or Mn. The potentially inaccurate Fe and Mn signals might enlarge REE concentrations in Fe/Mn (oxyhydr)oxides. Hence, we conducted an in-situ elemental analysis using EPMA and LA-ICP-MS, which yielded more accurate concentration.

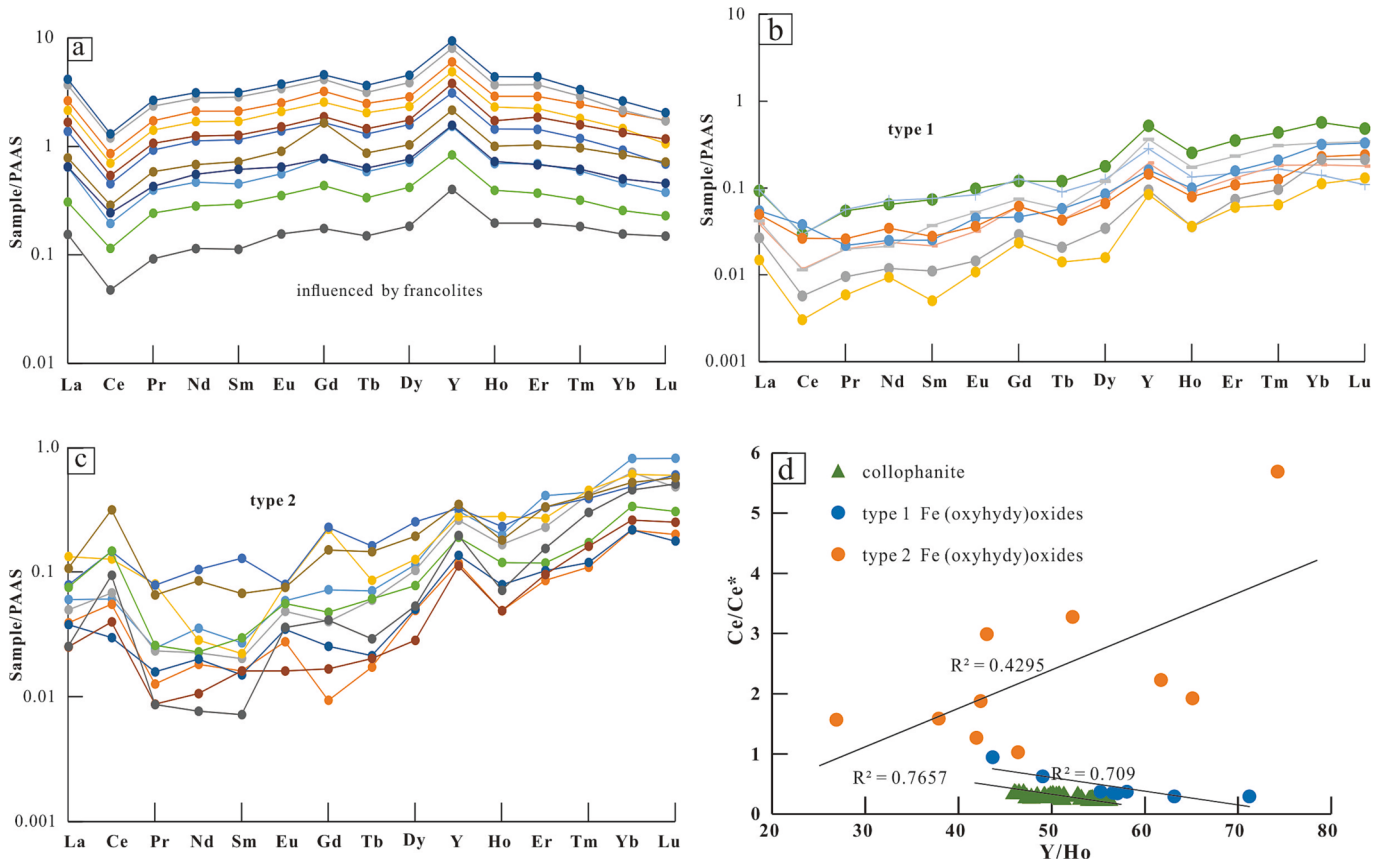

Fig. 10. PAAS-normalized REE patterns (a-c) and the relationships between Ce/Ce* and Y/Ho ratios (d) of Fe (oxyhydr)oxides from the Gezhongwu Formation. PAAS data came from Taylor and McLennan (1985). Partial Fe (oxyhydr)oxides were influenced by francolites (a) and two types (1, 2) of true REE patterns were recognized (b, c).

4.3. REE compositions of Fe (oxyhydr)oxides: Fe (oxyhydr)oxide origins

Tables 5 and 6 list the in-situ geochemical compositions of Fe (oxyhydr)oxides. In-situ major elements showed that Fe (oxyhydr)oxides have FeO levels between 66.16 % and 82.84 % (mean of 73.66 %, Table 5). The data showed that FeO levels in the Fe (oxyhydr)oxide rim (mean of 75.32 %) were much higher than those in the core (mean of 72.18 %). This supports a gradual Fe mineral phases transformation from the rim to the core.

The elemental concentrations, especially REE compositions, showed three types of Fe (oxyhydr)oxides, however, one of them were influenced by francolites because of higher amounts of P_2O_5 and CaO (Table 6). This type Fe (oxyhydr)oxide had the mean ∑REE of 367.63 ppm, negative Ce anomalies, positive Y anomalies, and a "hat-shaped" REE plot (Fig. 10a). Therefore, it was excluded for Fe (oxyhydr)oxide origin discussions. Whereas, other two types of Fe (oxyhydr)oxides represent true values: (1) type 1 had ∑REE ~ 19.74 ppm, weakly to markedly negative Ce anomalies, positive Y anomalies, and a "seawater-like" REE plot (Fig. 10b); (2) type 2 had ∑REE of ~ 28.29 ppm, positive Ce and Y anomalies, negative to positive Eu, Nd, Sm, Gd, and Er anomalies, and a "left-inclined" REE plot (Fig. 10c). Generally, Y/Ho ratios negatively correlated with Ce/Ce* in type 1 Fe (oxyhydr)oxides, while a positive correlation was observed in type 2 Fe (oxyhydr)oxides (Fig. 10d). Diluting minerals in modern deep-sea water, including carbonates and quartz, contain scarce REEs (Kato et al., 2011; Kashiwabara et al., 2018). Previous research reported that low levels of ∑REE (~50 ppm) in dolomite (Yang et al., 2021b). Our results showed that Fe (oxyhydr)oxides contained ∑REE ~ 20 ppm, excluded from the host minerals of REEs. Therefore, excluding these objects, francolites were mainly REE-hosted minerals, containing ∑REE concentrations up to 3000 ppm (Yang et al., 2022a).

Origins of Fe (oxyhydr)oxides are identified according to in-situ REE compositions. Usually, Fe/Mn (oxyhydr)oxides are classified as hydrothermal, hydrogenic, diagenetic, and mixed origins (Mills et al., 2001; Xiao et al., 2017). Due to different formation conditions, the geochemical compositions differ significantly from each other, especially in REE compositions (Prakash, 2012; Xiao et al., 2017). Previous research showed that hydrothermal Fe/Mn (oxyhydr)oxides were characterized by negative Ce, positive Eu, and positive Y anomalies and HREE enrichment (Fig. 11a) (Olivarez and Owen, 1991; Prakash, 2012; Xiao et al., 2017). In contrast, hydrogenic Fe (oxyhydr)oxides precipitated as crust or nodules through normal seawater sedimentation. In hydrogenic conditions, REEs were fractionated due to partition coefficients, in which Fe (oxyhydr)oxides absorbed Ce and HREE preferentially and discriminated against Y, which caused "left-inclined" REE plots with positive Ce and negative Y anomalies (Fig. 11a) (Ohta and Kawabe, 2001; Haley et al., 2004; Bau and Koschinsky, 2009; Xiao et al., 2017). Diagenetic Fe (oxyhydr)oxides, always related to hydrogenic nodules, showed similar REE patterns with hydrogenic Fe (oxyhydr)oxides except for negative Ce anomalies (Fig. 11a) (Bau et al., 2014; Xiao et al., 2017). Compared to this, type 1 and 2 Fe (oxyhydr)oxides showed mixed hydrothermal and hydrogenic origins based on their negative to positive Ce and Eu anomalies, positive Y anomalies, and "left-inclined" REE patterns (Fig. 11). Furthermore, Ce/Ce* vs. $(Y/Ho)_{SN}$ and Ce/Ce* vs. Nd graphs distinguished genetic types of Fe/Mn (oxyhydr)oxides (Bau et al., 2014). In the discriminant figures, type 1 Fe/Mn (oxyhydr)oxides from Zhijin phosphorite were located in hydrothermal areas. In contrast, type 2 was located outside these areas and showed mixed characteristics of hydrothermal and hydrogenic origins (Fig. 11b, c).

We infer that weakly positive Eu anomalies might be resulted from

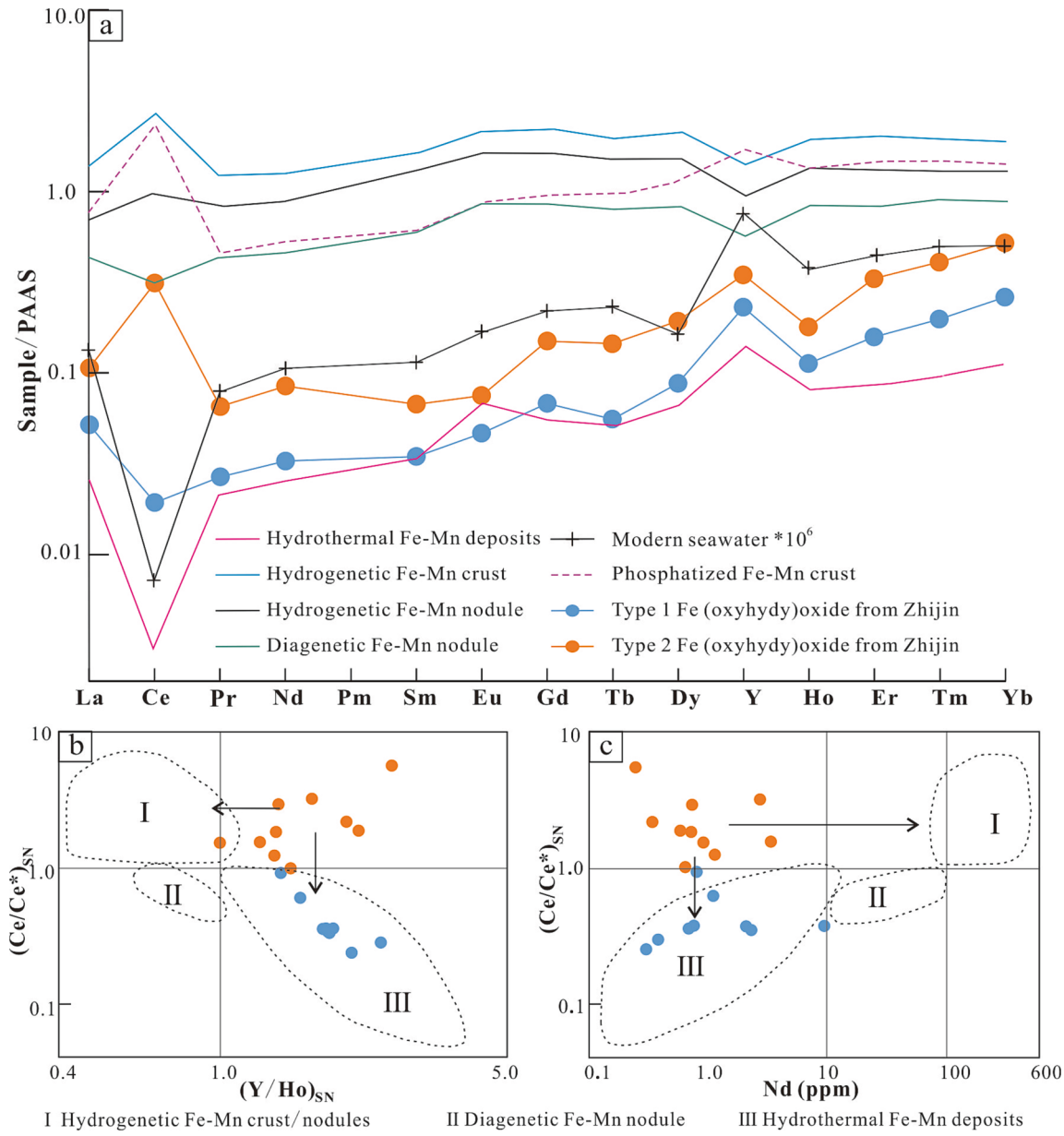

Fig. 11. PAAS-normalized REE patterns of different genetic Fe/Mn oxyhydroxide precipitates and modern seawater (a) and binary discriminant graph of $(Ce/Ce^*)_{SN}$ vs. $(Y/Ho)_{SN}$ (b) and $(Ce/Ce^*)_{SN}$ vs. Nd concentration (c) of Zhijin Fe (oxyhydr)oxides. Fe/Mn oxyhydroxide precipitates were taken from Bau et al. (2014) and seawater were from Alibo and Nozaki (1999). The binary discriminant graph was taken from Xiao et al. (2017), and boundaries of fields I, II, and III were demarcated based on data distributions from Bau et al. (2014).

later hydrothermal events rather than hydrothermal origins. The evidence came from the irrelevance between Eu/Eu* and Fe/Mn concentrations in bulk rocks (Fig. 12). Relative stabilities of aqueous Eu^{2+} and Eu^{3+} are associated closely with temperature, redox, and diagenesis. Even though the Eu valence changes based on the redox conditions, the Eu fractionation from other REEs was extremely feeble (Holser, 1997). Temperature is an essential factor for Eu fractionation. Under high temperatures (>250 °C) and high pressures, Eu^{2+} ions predominate and are scavenged by Fe/Mn (oxyhydr)oxides disproportionately relative to its neighbors, which causes apparent positive anomalies in hydrothermal fluids and sediments (Olivarez and Owen, 1991; Bau and Dulski, 1995; Poulton and Canfield, 2006). At lower temperatures (closer to surface temperatures), Eu^{2+} predominates and positive Eu comes from Eu^{2+} entering into crystal lattices, such as carbonates, organic-rich rocks, and diagenetic sediments (Martinez et al., 1999; Kidder et al., 2003; Yang et al., 2021b). Therefore, on the condition that Fe/Mn (oxyhydr)oxides come from hydrothermal fluids, Fe and Mn concentrations should correlate positively with Eu/Eu* in sediments. However, in the Zhijin phosphorite deposit, Eu/Eu* did not correlate with TFe and MnO_2 (Fig. 12), which implied that positive Eu/Eu* might be caused by later hydrothermal events rather than Fe/Mn (oxyhydr)oxides coming from hydrothermal fluids. Furthermore, Olivarez and Owen (1991) examined hydrothermal sediments from the southwest Pacific Ocean and those results showed Eu/Eu* became more seawater-like with increasing distance to the ridge axis. It indicated that Fe (oxyhydr)oxides were highly efficient scavengers of Eu in hydrothermal conditions, whereas Eu scavenged from seawater precipitation does not exhibit positive anomalies (Olivarez and Owen, 1991). Therefore, no to weakly positive Eu anomalies in the Fe (oxyhydr)oxides from the Zhijin phosphorites could be driven by seawater scavenging Eu, and then altered weakly by later hydrothermal events.

The difference between types 1 and 2 Fe (oxyhydr)oxides comes from

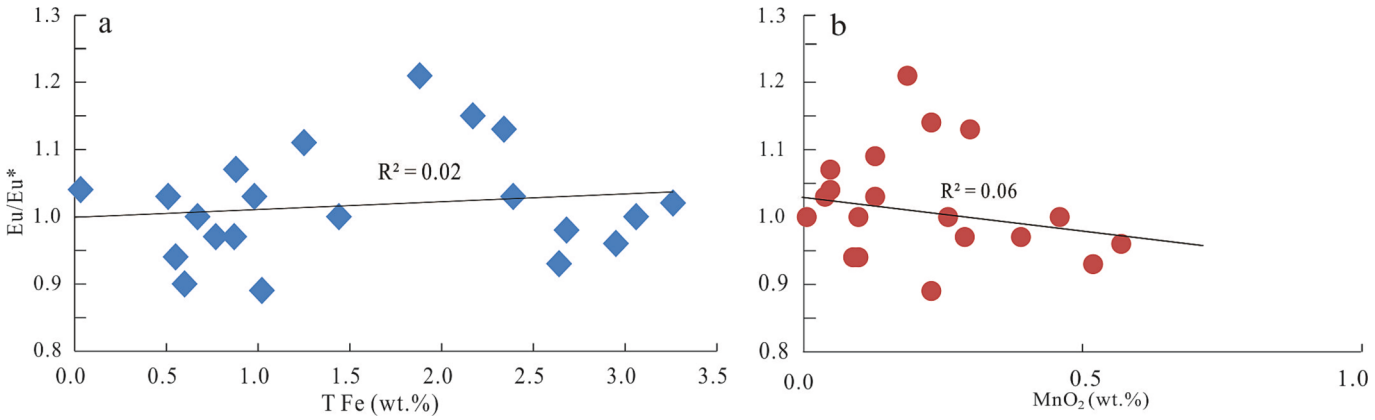

Fig. 12. Relationships between Eu/Eu* and total Fe (TFe) (a) and MnO_2 (b) of bulk phosphorite rocks from the Zhijin deposit.

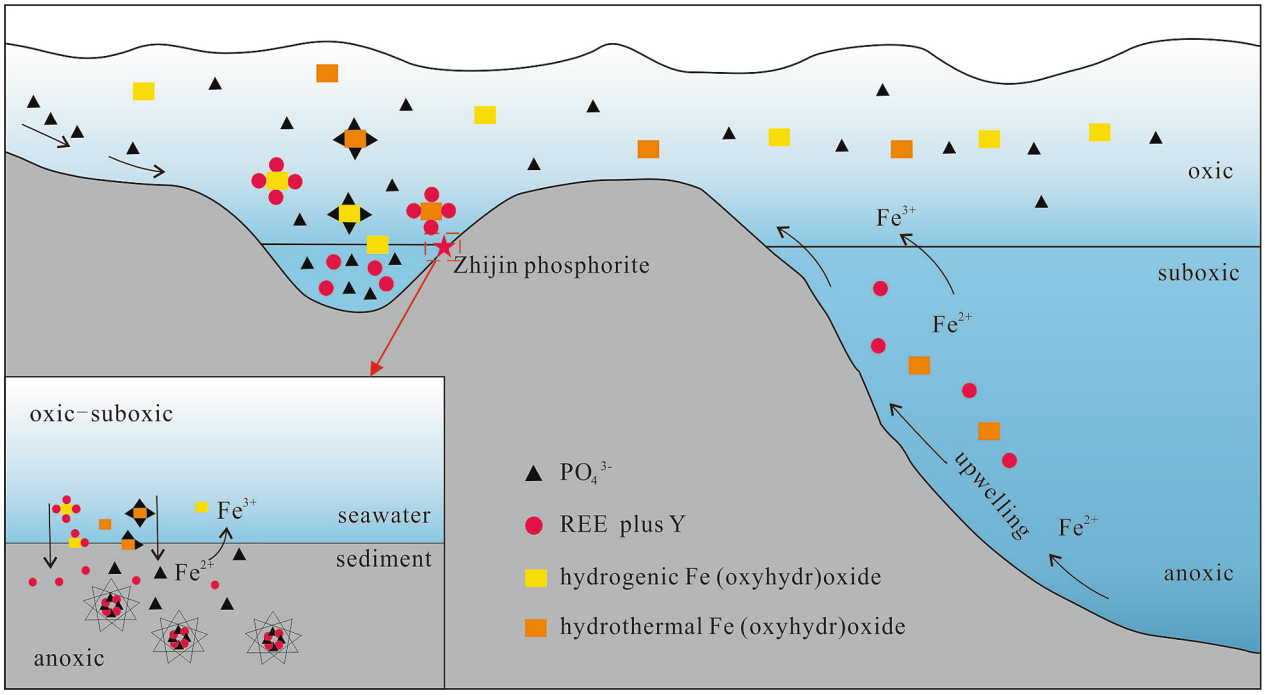

Fig. 13. Diagram of REE enrichment controlled by Fe redox cycle in Zhijin phosphorites.

Ce anomalies and Y/Ho ratios (Fig. 10d), attributed to redox fluctuations and later hydrothermal alteration, respectively.

On one hand, a positive correlation between Ce/Ce* and Y/Ho in type 2 Fe (oxyhydr)oxides might be caused by seawater and diagenesis redox fluctuations. Previous research suggested that Ce was oxidized to insoluble CeO_2 and absorbing onto the Fe/Mn (oxyhydr)oxide surface, depleting Ce in seawater (Holser, 1997; Pourret et al., 2008). However, other work showed oxidation of dissolved Ce(III) did not occur prior to Ce removal from seawater column, but after its sorption onto the Fe/Mn (oxyhydr)oxide surface (Ohta and Kawabe, 2001; Bau and Koschinsky, 2009). Regardless, the Ce anomalies were most closely associated with preferential scavenging by Fe and/or Mn (oxyhydr)oxides (Ohta and Kawabe, 2001; Pourret et al., 2008; Bau and Koschinsky, 2009; Bau et al., 2014; Xiao et al., 2017). Despite the distinct surface complexation between Fe/Mn (oxyhydr)oxides, positive Ce anomalies were caused by the same oxidation scavenging process (Ohta and Kawabe, 2001; Bau and Koschinsky, 2009; Prakash, 2012). Furthermore, Fe (oxyhydr)oxides preferentially adsorbed Ho relative to Y in oxic conditions due to the significantly higher marine particle reactivity of Ho in comparison to Y (Bau et al., 1997). This caused fractionation between Y and Ho and a lower Y/Ho ratio in Fe (oxyhydr)oxides (Bau, 1999; Bau and Koschinsky, 2009). However, under suboxic/anoxic diagenetic conditions, insoluble Ce(IV) was reduced to soluble Ce(III) and released into porewater, decreasing positive Ce anomalies in Fe (oxyhydr)oxides (Bau et al., 1997; Holser, 1997; Xiao et al., 2017). Under these suboxic/anoxic diagenetic conditions, Y/Ho ratios also increased due to lower stabilities of Y surface complexes relative to its REE neighbors (Bau et al., 1997). Therefore, positive Ce anomalies in type 2 Fe (oxyhydr)oxides were caused by seawater oxidation and a positive correlation between Ce/Ce* and Y/Ho resulted from diagenetic redox variations.

On another hand, the negative correlation between Ce/Ce* and Y/Ho in type 1 Fe (oxyhydr)oxides was caused by the mixing of hydrothermal fluids and seawater. Fe/Mn (oxyhydr)oxides formed in hydrothermal fluids had negative Ce and remarkable Y enrichment (Olivarez and Owen, 1991; Prakash, 2012; Xiao et al., 2017). When hydrothermal Fe/Mn (oxyhydr)oxides gradually mixed with seawater, negative Ce and positive Y anomalies decreased (Bau et al., 2014), which were characterized by a negative correlation between Ce/Ce* and Y/Ho, consistent with type 1 Fe (oxyhydr)oxides (Fig. 10d). Therefore, we infer that type 1 Fe (oxyhydr)oxides showed mixed hydrothermal and hydrogenic

characteristics, with negative Ce anomalies and high Y/Ho ratios overprinted by hydrothermal events after precipitation. As a result, in Zhijin phosphorites, two kinds of Fe (oxyhydr)oxides were observed: type 1 Fe (oxyhydr)oxides were mainly hydrothermal in origins while type 2 was mainly hydrogenic in origins.

4.4. Fe (oxyhydr)oxides participation in REE enrichment in francolites

A consensus on the influence of Fe/Mn (oxyhydr)oxides in francolite formation and REE enrichment has been reached (Bau et al., 1996; Yang et al., 2022a; Zhang et al., 2022). Highly-reactive Fe/Mn (oxyhydr)oxides acted as REE carriers in the sediments, confirmed by the REEs and Fe correlation in bulk rocks (Kato et al., 2011; Kashiwabara et al., 2018; Ren et al., 2022). On one hand, hydrothermal fluids provided the Fe/Mn (oxyhydr)oxides. Along with upwelling caused by transgressions or storm events (Liu et al., 1987; Mi, 2010), hydrothermal Fe/Mn (oxyhydr)oxides were brought into shallower seawaters. In Zhijin phosphorites, our previous discussion eliminated this possibility. On the other hand, Fe/Mn (oxyhydr)oxides participated in REE enrichment in francolites via a Fe-redox cycle. The following discussion will explore the REE-rich process associated with Fe/Mn (oxyhydr)oxides in Zhijin phosphorite.

In Zhijin phosphorites, Fe (oxyhydr)oxides participation in REE enrichment was controlled by redox variations, in which Fe (oxyhydr) oxides adsorbed REEs in oxic water and released them under suboxic/anoxic conditions (Fig. 13). Based on negative Ce anomalies in phosphorites and dolomites (Shi et al., 2004; Wu et al., 2022a; Yang et al., 2022a) and Mo and Fe isotopes, the early Cambrian ocean in South China was redox-stratified, comprising oxygenated shallow water and anoxic deep water (Wen et al., 2011; Fan et al., 2016a; Liu, 2017). Previous research indicated that the Zhijin phosphorite formed in oxic conditions (Liu, 2017; Yang et al., 2021a). A different viewpoint was proposed by Zhang et al. (2021), which suggested that Zhijin phosphorites recorded anoxic seawater conditions and oxic diagenetic conditions. Lumiste et al. (2021) recently conducted in-situ REE compositions on shelly phosphorites from the early Cambrian and found: (1) heterogeneous distribution of REE + Y in apatite, (2) diagenetic REE + Y compositions, and (3) variable pyrite levels. This implied that redox conditions differed across short distances during early diagenesis. Therefore, sedimentary and diagenetic redox conditions of Cambrian phosphorite were inconsistent. In the Zhijin deposit, distinct Ce anomalies and Y/Ho ratios in Fe(oxyhydr)oxides responded to oxic seawater and variable redox diagenetic conditions. Under these conditions, iron existed as Fe (III) (oxyhydr)oxides in the oxic water column (Shaffer, 1986). As a result, REEs, especially Ce, were preferentially adsorbed and produced positive Ce anomalies in Fe (oxyhydr)oxides (Ohta and Kawabe, 2001; Pourret et al., 2008; Bau and Koschinsky, 2009). After precipitation under the suboxic-anoxic water–sediment interface, Fe (III) was reduced as Fe(II), which released REEs into the porewater (Haley et al., 2004). This process, called Fe-redox pumping, significantly enriched REEs in porewater (Elderfield and Sholkovitz, 1987; Haley et al., 2004; Takahashi et al., 2015; Zhang et al., 2022). Subsequently, francolites formed and captured REEs during early diagenesis, which was recently confirmed by Fe isotopes and reported by Zhang et al. (2022).

Yang et al., (2022a) compared recent phosphate sediments and ancient phosphorites and suggested that recent francolites could serve as predecessors of major ancient phosphorites. If true, the same processes that Fe/Mn (oxyhydr)oxides participated in REE enrichment in francolites were expected to occur in early Cambrian phosphorites (Haley et al., 2004; Lumiste et al., 2019; Yang et al., 2022a). In modern deep-sea hydrothermal sediment areas (Fe-Mn-enriched), ∑REE has prominent positive relationships with sedimentary francolites (Kashiwabara et al., 2018). Whereas, porewaters with dissolved Fe generally contain REE concentrations much higher than porewater without dissolved Fe (Haley et al., 2004). This indicated that modern Fe/Mn (oxyhydr)oxide particles adsorbed REEs and were released them into porewaters, which caused REE enrichment (Elderfield and Sholkovitz, 1987; Haley et al., 2004; Takahashi et al., 2015). As a result, we concluded that Fe (oxyhydr)oxides played a role in REE enrichment in francolites under fluctuant redox conditions in not only recent francolites but also old phosphorites.

A conclusion acquired according to the discussion above entered on the roles Fe/Mn (oxyhydr)oxides played in REE enrichment in phosphorites. However, it might be magnified because there were lower REE levels in Fe (oxyhydr)oxides. In this study, ∑REE in Zhijin Fe(oxyhydr) oxides reached only 28 ppm, even ∑REE in Fe (oxyhydr)oxides influenced by francolites was 270 ppm on average (Table 6). Zhang et al. (2022) conducted in-situ elemental analyses of Fe oxides from the early Cambrian that ranged from 10 to 20 ppm, consistent with our results. Furthermore, REE compositions of Fe(oxyhydr)oxides might be altered during oxidation and/or weathering, which led to the in-situ analysis inaccuracies. Hence, even though our results support Fe/Mn (oxyhydr) oxide participation REE enrichment in francolites, more research and in-depth explanations are still needed to reveal the roles of Fe/Mn (oxyhydr)oxides.

5. Conclusions

To determine the role that Fe/Mn (oxyhydr)oxides played in REE enrichment in marine phosphorites, the mineralogical properties of Fe/Mn (oxyhydr)oxides in early Cambrian phosphorites from Zhijin, South China were investigated. Only the geochemical analysis of Fe (oxyhydr) oxides was conducted due to the flocculent textures of Mn (oxyhydr) oxides, and this study drew the following conclusions:

(1) Findings confirmed that REEs were mainly hosted in francolites rather than in dolostone and Fe/Mn (oxyhydr)oxides. Two kinds of Fe (oxyhydr)oxides were observed: Fe (oxyhydr)oxide individuals and Fe (oxyhydr)oxides composed of gray rim and bright core. SEM-EDS and laser Raman showed that Fe (oxyhydr)oxides transformed from hematite to goethite during the oxidation and/or weathering. The core of Fe (oxyhydr)oxides and Fe (oxyhydr)oxide individuals might provide information about REE enrichment in phosphorites.

(2) Two types of REE patterns in Fe (oxyhydr)oxides were distinguished. Both had “left-inclined” plots, positive Y anomalies, and negative to positive Eu anomalies, with the differences came from Ce anomalies. Type 1 Fe (oxyhydr)oxides showed hydrothermal in origin with diagenetic redox variations, while type 2 Fe (oxyhydr)oxides were hydrogenic origin mixed hydrothermal alteration. According to the irrelevance between Fe/Mn concentrations and Eu/Eu* in bulk rocks, we inferred that Fe (oxyhydr)oxides were altered by later hydrothermal events during diagenesis rather than deriving from hydrothermal fluids.

(3) The role Fe (oxyhydr)oxides played in REE enrichment in francolites was controlled by fluctuant redox conditions around the redox interface. During which, Fe (oxyhydr)oxides adsorbed REEs in an oxic water column and then released REEs in suboxic/anoxic porewaters, this process enriched the REE concentration in porewater. Subsequently, francolites formed and captured REEs during early diagenesis. This process might result in extraordinary REE resources in Zhijin early Cambrian phosphorites.

Declaration of Competing Interest

The authors declare that they have no known competing financial interests or personal relationships that could have appeared to influence the work reported in this paper.

Data availability

Data will be made available on request.

Acknowledgements

The authors are grateful to Prof. Zhuojun Xie and Dr. Qinping Tan for their helpful suggestions toward improving the quality of this manuscript. This work was supported by the National Natural Science Foundation of China [Grant Numbers: 92062221, 42202089, 41972095].

Appendix A. Supplementary material

Supplementary data to this article can be found online at https://doi.org/10.1016/j.jseaes.2023.105910.

References

Alibo, D.S., Nozaki, Y., 1999. Rare earth elements in seawater: Particle association, shale-normalization, and Ce oxidation. Geochim. Cosmochim. Acta 63 (3–4), 363–372.
Balaram, V., 2019. Rare earth elements: A review of applications, occurrence, exploration, analysis, recycling, and environmental impact. Geosci. Front. 10 (4), 1285–1303.
Bao, Z.W., Zhao, Z.H., 2008. Geochemistry of mineralization with exchangeable REY in the weathering crusts of granitic rocks in South China. Ore Geol. Rev. 33 (3–4), 519–535.
Bau, M., 1999. Scavenging of dissolved yttrium and rare earths by precipitating iron oxyhydroxide: Experimental evidence for Ce oxidation, Y-Ho fractionation, and lanthanide tetrad effect. Geochim. Cosmochim. Acta 63 (1), 67–77.
Bau, M., Dulski, P., 1995. Comparative study of yttrium and rareearth element behaviours in fluorine-rich hydrothermal fluids. Contrib. Mineral. Petrol. 119 (2–3), 213–223.
Bau, M., Dulski, P., 1996. Distribution of yttrium and rare-earth elements in the Penge and Kuruman iron-formations, Transvaal Supergroup, South Africa. Precambr. Res. 79 (1–2), 37–55.
Bau, M., Koschinsky, A., 2009. Oxidative scavenging of cerium on hydrous Fe oxide: Evidence from the distribution of rare earth elements and yttrium between Fe oxides and Mn oxides in hydrogenetic ferromanganese crusts. Geochem. J. 43 (1), 37–47.
Bau, M., Koschinsky, A., Dulski, P., Hein, J.R., 1996. Comparison of the partitioning behaviours of yttrium, rare-eatrh elements, and titanium between hydrogenetic marine ferromangaese crust ans seawater. Geochemica Et Cosmochimica ACTA. 60 (10), 1709–1725.
Bau, M., Möller, P., Dulski, P., 1997. Yttrium and lanthanides in eastern Mediterranean seawater and their fractionation during redox-cycling. Mar. Chem. 56 (1–2), 123–131.
Bau, M., Schmidt, K., Koschinsky, A., Hein, J., Kuhn, T., Usui, A., 2014. Discriminating between different genetic types of marine ferro-manganese crusts and nodules based on rare earth elements and yttrium. Chem. Geol. 381, 1–9.
Cook, P.J., 1992. Phosphogenesis around the Proterozoic Phanerozoic transition. J. Geol. Soc. London 149 (4), 615–620.
Cook, P.J., Shergold, J.H., 1984. Phosphorus, phosphorites and skeletal evolution at the Precambrian—Cambrian boundary. Nature 308 (5956), 231–236.
Cowie, J.W., Johnson, M.R.W., 1985. The chronology of the geological record. Geol. Soc. Lond, Mem.
Elderfield, H., Sholkovitz, E.R., 1987. Rare earth elements in the pore waters of reducing nearshore sediments. Earth Planet. Sci. Lett. 82 (3–4), 280–288.
Emsbo, P., McLaughlin, P.I., Breit, G.N., Bray, E.A.B., Koenig, A.E., 2015. Rare earth elements in sedimentary phosphate deposits: Solution to the global REE crisis? Gondw. Res. 27 (2), 776–785.
Fan, H.F., Wen, H.J., Zhu, X.K., 2016a. Marine Redox Conditions in the Early Cambrian Ocean: Insights from the Lower Cambrian Phosphorite Deposits, South China. J. Earth Sci. 27 (2), 282–296.
Fan, H.R., Yang, K.F., Hu, F.F., Liu, S., Wang, K.Y., 2016b. The giant Bayan Obo REE-Nb-Fe deposit, Chian: controversy and genesis. Geosci. Front. 7, 335–344.
Felitsyn, S., Morad, S., 2002. REE patterns in latest Neoproterozoic–early Cambrian phosphate concretions and associated organic matter. Chem. Geol. 187 (3–4), 257–265.
Francovschi, I., Gradinaru, E., Roban, R.D., Ducea, M.N., Ciobotaru, V., Shumlyanskyy, L., 2020. Rare earth element (REE) enrichment of the late Ediacaran Kalyus Beds (East European Platform) through diagenetic uptake. Geochemistry 80 (2). https://doi.org/10.1016/j.chemer.2020.125612.
Frei, R., Xu, L.G., Frederiksen, J.A., Lehmann, B., 2021. Signals of combined chromium-cadmium isotopes in basin waters of the Early Cambrian - Results from the Maoshi and Zhijin sections, Yangtze Platform, South China. Chem. Geol. 56 https://doi.org/10.1016/j.chemgeo.2021.120061.
Frezzotti, M.L., Tecce, F., Casagli, A., 2012. Raman spectroscopy for fluid inclusion analysis. J. Geochem. Explor. 112, 1–20.
Haley, B.A., Klinkhammer, G.P., McManus, J., 2004. Rare earth elements in pore waters of marine sediments. Geochim. Cosmochim. Acta 68 (6), 1265–1279.
Holser, W.T., 1997. Evaluation of the application of rare-earth elements to paleoceanography. Palaeogeogr. Palaeoclimatol. Palaeoecol. 132 (1–4), 309–323.
Horan, M.F., Morgan, J.W., Grauch, R.I., Coveney Jr., R.M., Murowchick, J.B., Hulbert, L.J., 1994. Rhenium and osmium isotopes in black shales and Ni-Mo-PGE-rich sulfide layers, Yukon-Territory, Canada, and Hunan and Guizhou Provinces. China. Geochimica Et Cosmochimica Acta. 58, 257–265.
Hurai, V., Huraiovà, M., Slobodnik, M., Thomas, R., 2015. Geofluids: Developments in Microthermometry, Spectroscopy, Thermodynamics and Stable Isotopes. Elsevier.
Jarvis, I., Burnett, W.C., Nathan, Y., Almbaydin, F.S.M., Attia, A.K.M., Castro, L.N., Flicoteaux, R., Hilmy, M.E., Husain, V., Qutawnah, A.A., Serjani, A., Zanin, Y.N., 1994. Phosphorite geochemistry—state-of-the-art and environmental concern. Eclogae Geol. Helv. 87, 643–700.
Jiang, S., Yang, J., Ling, H., Feng, H., Chen, Y., Chen, J., 2004. Re-Os isotopes and PGE geochemistry of black shales and intercalated Ni-Mo polymetallic sulfide bed from the Lower Cambrian Niutitang Formation, South China. Progr. Nat. Sci.-Mater. Int. 18–24.
Kashiwabara, T., Toda, R., Nakamura, K., Yasukawa, K., Fujinaga, K., Kubo, S., Nozaki, T., Takahashi, Y., Suzuki, K., Kato, Y., 2018. Synchrotron X-ray spectroscopic perspective on the formation mechanism of REY-rich muds in the Pacific Ocean. Geochim. Cosmochim. Acta 240, 274–292.
Kato, Y., Fujinaga, K., Nakamura, K., Takaya, Y., Kitamura, K., Ohta, J., Toda, R., Nakashima, T., Iwamori, H., 2011. Deep-sea mud in the Pacific Ocean as a potential resource for rare-earth elements. Nat. Geosci. 4 (8), 535–539.
Kidder, D.L., Krishnaswamy, R., Mapes, R.H., 2003. Elemental mobility in phosphatic shales during concretion growth and implications for provenance analysis. Chem. Geol. 198 (3–4), 335–353.
Kocsis, L., Trueman, C.N., Palmer, M.R., 2010. Protracted diagenetic alteration of REE contents in fossil bioapatites: Direct evidence from Lu-Hf isotope systematics. Geochemica Et Cosmochimica ACTA. 74 (21), 6077–6092.
Li, S. Y., Q, Y. X., Shen, J. F., Sun, L., Liu, B.,Yan, B. K. 2002. Source of Lower Cambrian platinum group elements in black shales in Hunan and Guizhou provinces, China and the Re-Os isotope dating. Sci. China (Series D). 32 568–575.
Li, Y.H.M., Zhao, W.W., Zhou, M.F., 2017. Nature of parent rocks, mineralization styles and ore genesis of regolith-hosted REE deposits in South China: An integrated genetic model. J. Asian Earth Sci. 148, 65–95.
Li, C.X., Zhou, M.F., 2015. Multiple stages of hydrothermal REE remobilization recorded in fluorapatite in the paleoproterozoic Yinachang Fe–Cu–(REE) deposit, Southwest China. Geochemica Et Cosmochimica ACTA. 166, 53–73.
Li, M.Y.H., Zhou, M.F., Williams-Jones, A.E., 2019. The genesis of regolith-hosted heavy rare earth element deposits: Insights from the world-class Zudong deposit in Jiangxi Province, South China. Econom. Geol. 114, 541–568.
Liu, K.W., 1989. The evolution of apatite inerals in the diagenetic processes. Acta Geol. Sin. 4 310–323+385-386 in Chinese with English abstract.
Liu, X. Q., Zhang, H., Tang, Y.,Long, L. Y. 2020. REE Geochemical Characteristic of Apatite: Implications for Ore Genesis of the Zhijin Phosphorite. Minerals. 10 (11): article # https://doi.org/10.3390/min10111012.
Liu, Y., Hou, Z.Q., Zhang, R.Q., Wang, P., Gao, J.F., Raschke, M.B., 2019. Zircon Alteration as a Proxy for Rare Earth Element Mineralization Processes in Carbonatite-Nordmarkite Complexes of the Mianning-Dechang Rare Earth Element Belt, China. Econom. Geol. 114 (4), 719–744.
Liu, Y.S., Hu, Z.C., Gao, S., Günther, D., Xu, J., Gao, C.G., Chen, H.H., 2008. In situ analysis of major and trace elements of anhydrous minerals by LA-ICP-MS without applying an internal standard. Chem. Geol. 257, 34–43.
Liu, B.J., Xu, X.S., Luo, A.P., Kang, C.L., 1987. Storm events and phosphate deposition in Cambrian on the western margin of the Yangtze platform, China. Acta Sedimentologica Sinica. 5 (3), 28–39 in Chinese with English abstract.
Liu, B.J., Xu, X.S., Xu, Q., Pan, X.N., Huang, H.Q., 1993. Sedimentary crustal evolution and mineralization of palaeocontinent in South China. Scientific Publications, Beijing, 236 pp (in Chinese).
Liu, Z.R.R., Zhou, M.F., 2017. Meishucun phosphorite succession (SW China) records redox changes of the early Cambrian ocean. Geol. Soc. Am. Bull. 129 (11–12), 1554–1567.
Liu, J., 2017. Mo isotopic signature of non-euxinic sediments and its paleo-oceanic significance. University of Chinese Academy of Sciences, Ph. D. Degree, 160 pp (in Chinese with English abstract).
Lumiste, K., Lang, L., Paiste, P., Lepland, A.,Kirsimäe, K. 2021. Heterogeneous REE + Y distribution in Early Paleozoic shelly phosphorites: Implications for enrichment mechanisms. Chem. Geol. 586 (30): article # https://doi.org/10.1016/j.chemgeo.2021.120590.
Lumiste, K., Mänd, K., Bailey, J., Paiste, P., Lang, L., Lepland, A., Kirsimäe, K., 2019. REE +Y uptake and diagenesis in Recent sedimentary apatites. Chem. Geol. 525 (20), 268–281.
Mao, J.W., Lehmann, B., Du, A.D., Zhang, G.D., Ma, D.S., Wang, Y.T., Zeng, M.G., Kerrich, R., 2002. Re-Os dating of polymetallic Ni-Mo-PGE-Au mineralization in lower Cambrian black shales of south China and its geologic significance. Econ. Geol. 97, 1051–1061.
Mao, T., Yang, R.D., 2013. Micro-structural charaterestics and composition of the small shelly fossils in Cambrian phosphorites, Zhijin. Guizhou. Acta Micropalaeontologica Sinica. 30 (2), 199–207 in Chinese with English abstract.
Martinez, R.F., Ortega, H.M., Palomo, I., 1999. Positive Eu anomaly development during diagenesis of the K/T boundary ejecta layer in the Agost section (SE Spain): implications for trace-element remobilization. Terra Nova 11 (6), 290–296.
Mi, W.T., 2010. Phosphorites Sedimentary Event in Sinian Doushantuo period, West Yangtze Area - the Cases Study of Weng'an Phosphorite in Guizhou and Yichang Phosphorite in Hubei. Chengdu Univ. Technol., Ph. D Degree 99 pp (in Chinese with English abstract.
Mills, R.A., Wells, D.M., Roberts, S., 2001. Genesis of ferromanganese crusts from the TAG hydrothermal field. Chem. Geol. 176 (1–4), 283–293.
Nie, D.P., 2018. Occurrence state and behavior of rare earth in acid/pyrolysis process of rare earth rich phosphate ore in Zhijin, Guizhou. Guizhou Univ., PhD Thesis 95 pp (in Chinese with English abstract.

Ohta, A., Kawabe, I., 2001. REE(III) adsorption onto Mn dioxide (delta-MnO2) and Fe oxyhydroxide: Ce(III) oxidation by delta-MnO2. Geochim. Cosmochim. Acta 65 (5), 695–703.
Olivarez, A.M., Owen, R.M., 1991. The europium anomaly of seawater: implications for fluvial versus hydrothermal REE inputs to the oceans. Chem. Geol. 92 (4), 317–328.
Papineau, D., 2010. Global Biogeochemical Changes at Both Ends of the Proterozoic: Insights from Phosphorites. Astrobiology 10 (2), 165–181.
Poulton, S.W., Canfield, D.E., 2006. Co-diagenesis of iron and phosphorus in hydrothermal sediments from the southern East Pacific Rise: Implications for the evaluation of paleoseawater phosphate concentrations. Geochim. Cosmochim. Acta 70 (23), 5883–5898.
Pourret, O., Davranche, M., Gruau, G., Dia, A., 2008. New insights into cerium anomalies in organic-rich alkaline waters. Chem. Geol. 251 (1–4), 120–127.
Prakash, 2012. Distribution of REEs and yttrium among major geochemical phases of marine Fe–Mn-oxides: comparative study between hydrogenous and hydrothermal deposits. Chem. Geol. 312–313, 127–137.
Pufahl, P.K., Groat, L.A., 2017. Sedimentary and igneous phosphate deposits: formation and exploration: An invited Paper. Econ. Geol. 112 (3), 483–516.
Pufahl, P.K., Hiatt, E.E., 2012. Oxygenation of the Earth's atmosphere-ocean system: A review of physical and chemical sedimentologic responses. Mar. Pet. Geol. 32 (1), 1–20.
Qi, L., Hu, J., Gregoire, D.C., 2000. Determination of trace elements in granites by inductively coupled plasma mass spectrometry. Talanta 51 (3), 507–513.
Ren, J.b., Jiang, X.X., He, G.W., Wang, F.L., Yang, T.B., Luo, S.J., Deng, Y.N., Zhou, J.H., Deng, X.G., Yao, H.Q., Yu, H.X., 2022. Enrichment and sources of REY in phosphate fractions: Constraints from the leaching of REY-rich deep-sea sediments. Geochemica Et Cosmochimica ACTA. 335, 155–168.
Shaffer, G., 1986. Phosphate pumps and shuttles in the Black Sea. Nature 321 (6069), 515–517.
She, Z.B., Strother, P., McMahon, G., Nittler, L.R., Wang, J.H., Zhang, J.H., Sang, L.K., Ma, C.Q., Papineau, D., 2013. Terminal Proterozoic cyanobacterial blooms and phosphogenesis documented by the Doushantuo granular phosphorites I: In situ micro-analysis of textures and composition. Precambr. Res. 235, 20–35.
Shi, C.H., 2005. Formation of phosphorite deposit, Breakup of Rodinia supercontinent and Biology explosion- A case study of Weng'an, Kaiyang and Zhijin phosphorite deposits of Guizhou Province. Univ. Chin. Acad. Sci. Ph. D. thesis, 108 pp (in Chinese with English abstract).
Shi, C.H., Hu, R.Z., Wang, G.Z., 2004. Study on REE geochemistry of Zhijin phosphorites, Guizhou province. J. Mineral. Petrol. 24 (4), 71–75 in Chinese with English abstract.
Shu, L.S., 2012. An analysis of principal features of tectonic evolution in South China Block. Geol. Bull. China 31 (7), 1035–1053 in Chinese with English abstract.
Steiner, M., Wallis, E., Ertman, B.D., Zhao, Y.L., Yang, R.D., 2001. Submarine hydrothermal exhalative ore layers in black shales from South China and associated fossils insights into Lower Cambrian facies and bio-evolution. Palaeogeogr. Palaeoclimatol. Palaeoecol. 169 (3–4), 165–169.
Steiner, M., Li, G., Qian, Y., Zhu, M., Erdtmann, B.-D., 2007. Neoproterozoic to early Cambrian small shelly fossil assemblages and a revised biostratigraphic correlation of the Yangtze Platform (China). Palaeogeogr. Palaeoclimatol. Palaeoecol. 254 (1–2), 67–99.
Takahashi, Y., Hayasaka, Y., Morita, K., Kashiwabara, T., Nakada, R., Marcus, M.A., Kato, K., Tanaka, K., Shimizu, H., 2015. Transfer of rare earth elements (REE) from manganese oxides to phosphates during early diagenesis in pelagic sediments inferred from REE patterns, X-ray absorption spectroscopy, and chemical leaching method. Geochem. J. 49 (6), 653–674.
Taylor, S.R., McLennan, S.M., 1985. The Continental Crust: Its Composition and Evolution, An Examination of the Geochemical Record Preserved in Sedimentary Rocks. Blackwell Scientific Publications, Oxford, p. 312 pp..
Wang, J., Li, Z.X., 2003. History of Neoproterozoic rift basins in South China: implications for Rodinia break-up. Precambr. Res. 122 (1), 141–158.
Wang, D.H., Zhao, Z., Yu, Y., Dai, J.J., Deng, M.C., Zhao, T., Liu, L.J., 2018. Exploration and research progress on ion-adsorption type REE deposit in South China. China Geol. 1 (3), 415–424.
Wen, H.J., Carignan, J., Zhang, Y.X., Fan, H.F., Cloquet, C., Liu, S.R., 2011. Molybdenum isotopic records across the Precambrian-Cambrian boundary. Geology 39 (8), 775–778.
Wright, J., Schrader, H., Holser, W.T., 1987. Paleoredox variations in ancient oceans recorded by rare earth elements in fossil apatite. Geochim. Cosmochim. Acta 51 (3), 631–644.
Wu, S.W., Fan, H.F., Xia, Y., Meng, Q.T., Gong, X.X., He, S., Liu, X.Q., Yang, H.Y., Wen, H.J., 2022a. Sources of rare earth elements and yttrium in the early Cambrian phosphorites in Zhijin, southwest China. Ore Geol. Rev. 150 https://doi.org/10.1016/j.oregeorev.2022.105146.
Wu, X.H., Han, Z.J., Cai, J.F., 1999. Guizhou phosphorite. Geological Publishing House, Beijing, 339 pp (in Chinese with English abstract.
Wu, S.W., Yang, H.Y., Fan, H.F., Xia, Y., Meng, Q.T., He, S., Gong, X.X., 2022b. Assessment of the Effect of Organic Matter on Rare Earth Elements and Yttrium Using the Zhijin Early Cambrian Phosphorite as an Example. Minerals. 12 (876) https://doi.org/10.3390/min12070876.
Xiao, J., He, J., Yang, H., Wu, C., 2017. Comparison between Datangpo-Type Manganese Ores and Modern Marine Ferromanganese Oxyhydroxide Precipitates Based on Rare Earth Elements. Ore Geol. Rev. 89, 290–308.
Xing, J.Q., Jiang, Y.H., Xian, H.Y., Zhang, Z.Y., Yang, Y.P., Tan, W., Liang, X.L., Niu, H. C., He, H.P., Zhu, J.X., 2021. Hydrothermal activity during the formation of REY-rich phosphorites in the early Cambrian Gezhongwu Formation, Zhijin, South China: A micro- and nano-scale mineralogical study. Ore Geol. Rev. 136 article # doi: 10.1016/j.oregeorev.2021.104224.
Xu, L.G., Lehmann, B., Mao, J.W., Qu, W.J., Du, A.D., 2011. Re-Os age of polymetallic Ni-Mo-PGE-Au mineralization in early Cambrian black shales of South China - a reassessment. Econ. Geol. 106 (3), 511–522.
Yang, H. Y., Xiao, J. F., Xia, Y., Xie, Z. J., Tan, Q. P., Xu, J. B., He, S., Wu, S. W., Liu, X. Q., Gong, X. X. 2021a. Phosphorite generative processes around the Precambrian-Cambrian boundary in South China: An integrated study of Mo and phosphate O isotopic compositions. Geosci. Front. 12 (5): article # https://doi.org/10.1016/j.gsf.2021.101187.
Yang, J.D., Sun, W.G., Wang, Z.Z., Wang, Y.X., 1996. Sm-Nd isotopic age of Precambrian Cambrian boundary in China. Geol. Mag. 133 (1), 53–61.
Yang, H.Y., Zhao, Z.F., Xia, Y., Xiao, J.F., 2021b. REY enrichment mechanisms in the early Cambrian phosphorite from South China. Sed. Geol. 426 https://doi.org/10.1016/j.sedgeo.2021.106041.
Yang, H.Y., Xiao, J.F., Xia, Y., Zhao, Z.F., Xie, Z.J., He, S., Wu, S.W., 2022a. Diagenesis of Ediacaran – early Cambrian phosphorite: Comparisons with recent phosphate sediments based on LA-ICP-MS and EMPA. Ore Geol. Rev. 144 https://doi.org/10.1016/j.oregeorev.2022.104813.
Yang, H.Y., Zhao, Z.F., Cao, X.M., Fan, H.F., Xiao, J.F., Xia, Y., Zeng, M., 2022b. Geochemistry of apatite individuals in Zhijin phosphorites, South China: Insight into the REY sources and diagenetic enrichment. Ore Geol. Rev. 150 https://doi.org/10.1016/j.oregeorev.2022.105169.
Ye, L.J., Chen, Q.Y., Liu, K.W., 1989. Chinese phosphorite rock. Science Press, Beijing, 339 pp (in Chinese).
Ye, X.T., Zhu, W.G., Zhong, H., He, D.F., Ren, T., Bai, Z.J., Fan, H.P., Hu, W.J., 2013. Zircon U-Pb and chalcopyrite Re-Os geochronology, REE geochemistry of the Yinachang Fe-Cu-REE deposit in Yunnan Province and its geological significance. Acta Petrol. Sin. 29 (4), 1167–1186.
Yuan, Z.X., Li, J.K., Wang, D.H., Zhen, G.D., Lou, D.B., Chen, Z.H., Zhao, Z., Yu, Y., 2012. Metallogenic regularity of rare earth deposits in China. Geological publishing house (Beijing), Beijin, p. 117.
Zhang, H.J., Fan, H.F., Wen, H.J., Han, T., Zhou, T., Xia, Y., 2022. Controls of REY enrichment in the early Cambrian phosphorites. Geochim. Cosmochim. Acta 324, 117–139.
Zhang, Z.Y., Jiang, Y.H., Niu, H.C., Xing, J.Q., Yan, S., Li, A., Weng, Q., Zhao, X.C., 2021. Enrichment of rare earth elements in the early Cambrian Zhijin phosphorite deposit, SW China: Evidence from francolite micro-petrography and geochemistry. Ore Geol. Rev. 138 article # doi: 10.1016/j.oregeorev.2021.104342.
Zhang, G.W., Li, S.Z., Dong, Y.P., Liu, S.F., He, D.F., Cheng, S.Y., Lu, R.K., Yao, A.P., 2013. Structure and the problems of the South China continent. Chin. Sci. Bull. 3, 1553–1582 in Chinese with English abstract.
Zhang, J., Zhang, Q., Chen, D.L., 2003. REE geochemistry of the Ore-bearing REE in Xinhua phosphorite, Zhijin, Guizhou. J. Mineral. Petrol. 23 (3), 35–38 in Chinese with English abstract.
Zhou, M.F., Li, M.Y.H., Wang, Z., Li, X.C., Liu, J., 2020. The genesis of regolith-hosted rare earth element and scandium deposits: Current understanding and outlook to future prospecting. Chin. Sci. Bull. 65, 3809–3824.
Zhu, M.Y., Zhang, J.M., Yang, A.H., 2007. Integrated Ediacaran (Sinian) chronostratigraphy of South China. Palaeogeogr. Palaeoclimatol. Palaeoecol. 254 (1–2), 7–61.